Geophysical Journal International

Geophys. J. Int. (2022) **228,** 958–981
Advance Access publication 2021 September 07
GJI Seismology

https://doi.org/10.1093/gji/ggab363

Rayleigh wave group velocity maps at periods of 10–150 s beneath South America

André Vinícius de Sousa Nascimento [1], George Sand França,[1] Carlos Alberto Moreno Chaves [2] and Giuliano Sant'Anna Marotta [1]

[1] *Observatório Sismológico, Instituto de Geociências, Universidade de Brasília, Prédio SG* 13 - *Campus Universitário Darcy Ribeiro - Asa Norte, Brasília, DF, Brazil. E-mail: andre_vinicius1@live.com*
[2] *Departamento de Geofísica, IAG, Universidade de São Paulo, Rua do Matão,* 1226 - *Cidade Universitária, São Paulo, SP* 05508-090, *Brazil*

Accepted 2021 September 2. Received 2021 August 25; in original form 2021 May 4

SUMMARY

Based on new data from permanent and temporary networks, we present fundamental mode Rayleigh wave group velocity maps at periods of 10–150 s related to the lithosphere beneath South America. We analyse waveform data from 1043 earthquakes, from 2002 to 2019, which were recorded by 282 stations. To isolate fundamental mode Rayleigh waves, a phase-matched filter is applied, and the measurements of group velocity are obtained from multiple filter analysis techniques. Thus, we obtain 17 838 paths, covering most of the South American continent, which reach their maximum at the period of 30 s and decrease for both shorter and longer periods. We calculate average dispersion curves and probability density distribution of all measured curves to check the consistency of our data set. Then, regionalized group velocity maps are obtained by iteratively combining the fast marching method and the subspace inversion method. The resolution of our models is assessed by checkerboard tests, which show that the synthetic group velocities are well recovered, despite some amplitude and smearing effects in some portions of the model, probably owing to regularization and uneven ray path coverage. Compared to previous group velocity studies for South America, our models present better resolution, mainly for shorter periods. Our maps of 10 and 20 s, for example, show an excellent correlation with the sedimentary thickness (CRUST1.0) and topography density (UNB_TopoDens). Regions of exposed basement and high-density are related to fast group velocities, while sedimentary basins and low-densities are observed as areas of slow group velocities. We identify small-scale fast group velocity heterogeneities that may be linked to the Rio Apa and Rio Tebicuary cratons as well as to the geochronological provinces of the Amazonian Craton. The most striking feature of our map at 40 s is a fast group velocity structure with the same NE trend of the Transbrasiliano lineament, a Neoproterozoic megashear fault that crosses a large part of the South American continent. Our long-period maps sample lithospheric depths, revealing that cratonic areas of South America, such as the Amazonian and São Francisco cratons, correlate well with fast group velocities. Another interesting feature is the presence of a strong group velocity gradient between the Paraná and Chaco-Paraná basins, which nearly coincides with the location of the Western Paraná Suture, a continental-scale gravity discontinuity. From our group velocity maps, we estimate 1-D *S*-wave velocity depth profiles at 10 locations in South America: Chaco-Tarija Basin, Borborema Province (BP), Amazonian Craton, Paraná Basin, Tocantins Province, Acre Basin (AcB), Altiplano-Puna Volcanic Complex, Mantiqueira Province (MP), Parnaíba Basin and São Francisco Craton. Most of our inverted *S*-wave velocity profiles show good agreement with the SL2013sv model at lithospheric depths, except the BP, AcB and MP profiles. Particularly for the BP, a low shear wave velocity, from about 75 to 150 km depth, is a feature that is not present in the SL2013sv model and was probably resolved in our model because of our denser ray path coverage. This decreased *S*-wave velocity may be due to a lithospheric thinning beneath the BP, as already pointed out by previous studies.

Key words: South America; Seismic tomography; Surface waves and free oscillations.

1 INTRODUCTION

The lithosphere of South America can be roughly divided into a relatively stable portion—the South American Platform, which occupies most of the continent—that is not affected by the Andean and Caribbean orogenesis and is surrounded by them; the Andean Phanerozoic Fold Belt on the west and north; and the Patagonian Block, a microcontinent with evolution independent from the rest of the continent, on its southern portion, bounded by the Andes to the west and by the Atlantic Ocean to the east (Almeida *et al.* 2000). Throughout geological time, the lithosphere of South America has been deformed and rearranged several times by Global Plate Tectonics processes. Thus, the basement of the continent is the result of a long evolution and may be considered the product of three main orogenic events: (i) the Trans-Amazonian, during the Palaeoproterozoic; (ii) the Late Mesoproterozoic and (iii) the Brasiliano/Pan-African, mainly in Neoproterozoic times (Almeida *et al.* 2000).

Due to a distinct tectonic evolution, the basement of the South American Platform can be divided into two main domains: a pre-Brasiliano N–NW Amazonian Domain, where large Archean nuclei are circumscribed by younger Palaeo- and Mesoproterozoic mobile belts, and a central-eastern 'Brasiliano' Domain, whose structural framework was intensely shaped by Neoproterozoic orogenic cycles, namely the Brasiliano/Pan African events (Brito Neves & Fuck 2014), which were diachronous and distributed over four pulses: (i) *ca*. 800–740 Ma, (ii) *ca*. 660–610 Ma, (iii) *ca*. 590–560 Ma and (iv) 520–500 Ma (Brito Neves *et al.* 2014). Brito Neves & Fuck (2014) also recognized that the crustal evolution of the Amazonian Domain shares many similarities with the ancient Laurentian continent, while the Brasiliano Domain presents affinities with Western Gondwana. Those domains seem to be separated by a megashear zone named Transbrasiliano Lineament (TBL), which extends even further to Africa (e.g. Santos *et al.* 2008). Although of secondary importance to the Amazonian Craton (AmC) and surroundings (Brito Neves & Fuck 2013), the Brasiliano events resulted in the current configuration of the tectonic provinces in the South American Platform and the youngest fold belts of the basement were formed during the Neoproterozoic (Almeida *et al.* 2000). The Neoproterozoic orogenic systems include the Mantiqueira Province (MP), along the Brazilian coast, the Tocantins Province (TP), in central Brazil, and the Borborema Province (BP), in NE Brazil. Three large phanerozoic intracratonic basins are present in the South American Platform: Paraná Basin (PB), to the southeast, Parnaíba Basin (PaB), to the northeast and Amazon Basin (AmB), to the north. The basement is exposed through two main cratonic blocks in the South American Platform: the AmC, to the north and the São Francisco Craton (SFC), to the east. The AmC is further divided into two main shields: the Guyana shield, to the north of the AmB and the Guaporé shield, to the south. Fig. 1 summarizes the main current tectonic provinces of South America.

Seismic tomography models are essential to our understanding of tectonics, allowing us to link the reworking of surface geological features with the dynamic evolution of the Earth's deep interior (e.g. Gurnis *et al.* 2000; Torsvik *et al.* 2006; Van der Meer *et al.* 2018). Most seismic tomography experiments are designed to invert a large data set of the traveltimes of a variety of seismic waves, which propagate inside the Earth from the energy released by earthquakes and are recorded as seismograms by seismic stations placed at Earth's surface. From the analysis of seismograms, it is possible to identify a multitude of seismic phases, which probe different parts of the Earth, carrying crucial information on its heterogeneous velocity structure.

A better view of the lithospheric velocity structure beneath South America has been tried by several body wave (compressional and shear wave) and surface wave tomography studies over the years. Seismic tomography models derived from body wave data to constrain the upper mantle velocity heterogeneities underneath the South American Platform are usually more restricted to specific regions. Studied areas, for example, include the PB (e.g. VanDecar *et al.* 1995; Schimmel *et al.* 2003; Rocha *et al.* 2011, 2019a; Affonso *et al.* 2021), the TP (e.g. Azevedo *et al.* 2015), the BP (e.g. Simões Neto *et al.* 2019), the SFC (e.g. Rocha *et al.* 2019b) and the Guaporé shield, in the AmC (e.g. Costa *et al.* 2020). However, the cited body-wave tomography experiments have only provided a faint view of the velocity structure within the lithosphere under the studied areas, which overall is still poorly constrained in South America.

The strong dispersive character of surface waves combined with the fact that they travel along the Earth's surface may provide a good sampling of Earth's shallow velocity structure. Thus, surface wave group velocity maps are an important tool to investigate lateral variations of crustal and upper mantle velocity structure, at both regional and global scales, and may provide useful information related to the evolution of continents. Regional surface wave models that comprise the whole continent (e.g. Silveira *et al.* 1998; Vdovin *et al.* 1999; Van der Lee *et al.* 2001; Feng *et al.* 2004, 2007; Heintz *et al.* 2005) have successfully mapped long-wavelength structures as low-velocity anomalies beneath the Andean chain, and as well as high-velocity anomalies under cratonic areas. Those studies show agreement on the large-scale structures to a certain extent, but due to the distinct data set and inversion schemes, they differ in terms of resolution, anomaly amplitude and geometry. Furthermore, important small-scale structures are absent or not well constrained due to poor path coverage and scarce station distribution. Compared to other continents, such as North America or Europe, seismic station coverage in South America has always been quite sparse, especially in regions with low population density and/or hard to access, like the Amazon rainforest. Nevertheless, this situation has been improving since 2011, with the deployment of several new stations in Brazil by the following institutions: University of São Paulo (USP), University of Brasília (UnB), University of Rio Grande do Norte (UFRN) and National Observatory (ON). Those stations constitute the Brazilian Seismographic Network (RSBR, Bianchi *et al.* 2018). A new project named 3-Basins project, funded by São Paulo State Research Foundation (FAPESP), also has recently deployed several new temporary seismic stations in the region of the PB, Chaco-Paraná (CB) and Pantanal (PtB) Basins, improving significantly the coverage in the southwestern South American Platform. Therefore, relative to previous regional studies in South America using surface wave tomography (e.g. Vdovin *et al.* 1999; Feng *et al.* 2004, 2007; Heintz *et al.* 2005), the recently deployed RSBR and temporary networks have provided a more homogeneous station distribution, especially in northern (i.e. the Amazon) and northeastern Brazil.

Taking advantage of the newly deployed permanent and temporary stations, mainly in Brazil, to provide new constraints on the lithosphere velocity structure underneath South America, in this study we derive higher resolution Rayleigh wave group velocity maps at periods of 10–150 s. Our group velocity maps are obtained from the analysis of fundamental mode Rayleigh waves, which are used to measure group velocity dispersion curves. We discuss in detail data and measurements in Section 2. Based on a new data set, which is three times larger than the number of dispersion curves derived by Feng *et al.* (2007), we use the fast marching method combined with the subspace inversion method to iteratively solve

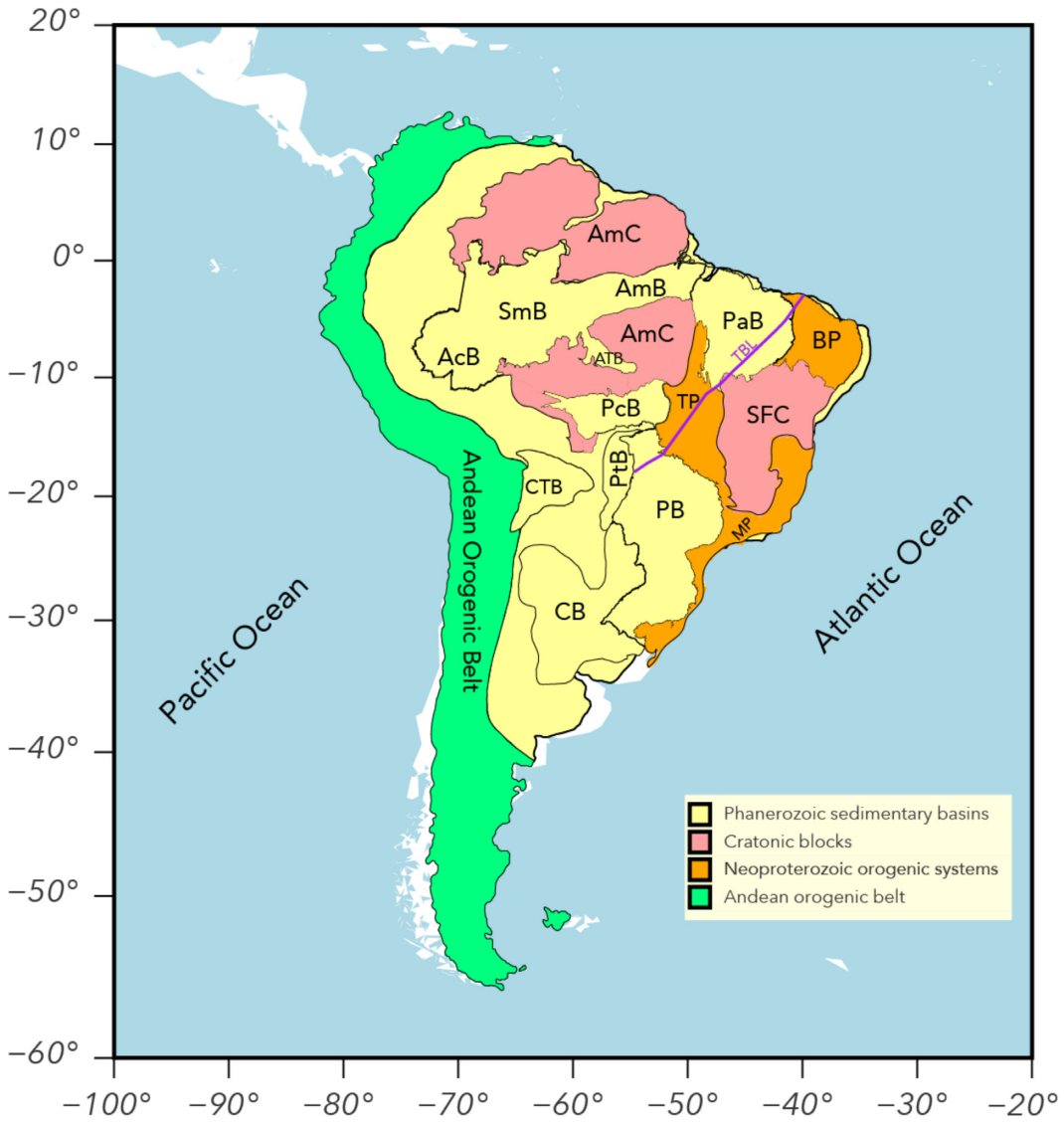

Figure 1. Main tectonic provinces of South America. The study area encompasses the Chaco-Paraná Basin (CB), Paraná Basin (PB), Pantanal Basin (PtB), Parnaíba Basin (PaB), Amazon Basin (AmB), Solimões Basin (SmB), Parecis Basin (PcB), Alto Tapajós Basin (ATB) Chaco-Tarija Basin (CTB), Acre Basin (AcB), Tocantins Province (TP), Borborema Province (BP), Mantiqueira Province (MP), São Francisco Craton (SFC), Amazonian Craton (AmC) and Transbrasiliano Lineament (TBL).

the forward and inverse steps in order to account for the non-linearity between traveltime and velocity. Our strategy to obtain 2-D regionalized group velocity maps and the checkerboard resolution tests is presented in Section 3 of this manuscript along with the derived group velocity maps. Despite some amplitude and smearing effects in some portions, the group velocity models are well recovered in our tests, with alternating anomaly patterns of 2° × 2°, 3° × 3°, 4° × 4° and 5° × 5°, respectively. We present 2-D Rayleigh wave group velocity maps for periods of 10, 20, 40, 50, 70, 100, 120 and 150 s, masking the oceanic areas since they are poorly sampled in this study. To inspect our tomographic images at different depths, we plot the sensitivity kernels of Rayleigh wave group velocities to shear wave velocities at different periods. In Section 4, we discuss the group velocity contribution to the imaging of the heterogeneous structure beneath the onshore area of South America. We show that our group velocity maps of 10 and 20 s present an excellent agreement with the sedimentary thickness (CRUST1.0, Laske *et al.* 2013) and topography density (UNB_TopoDens, Sheng *et al.* 2019) models, with fast group velocities related to the exposed basement and high-density topography, and slow group velocities related to the sedimentary basins and low-density topography. The AmC geochronological provinces are observed as areas of fast group velocities. Our map of 40 s shows a remarkable correlation between a fast group velocity structure with a NE trend and the Transbrasiliano Lineament, a Neoproterozoic megashear fault crossing Brazil. A strong velocity gradient between the PB and CB, which roughly coincides with the location of the Western Paraná Suture (WPS) is present on our maps of 100 and 150 s. Preliminary inversions of our 2-D regionalized maps for 1-D shear-wave velocity depth profiles are also provided at ten locations. In general, our inverted *S*-profiles are consistent with the SL2013sv model (Schaeffer & Lebedev 2013), except the BP, AcB and MP profiles. For the BP, for example, a lower *S*-wave velocity than the AK135 model (Kennett *et al.* 1995) at a depth from about 75 to 150 km is

observed and is not detected by the SL2013sv model. This result can support the hypothesis of lithospheric thinning beneath the BP, as evidenced by previous studies. Finally, in Section 5 we present our conclusions.

2 DATA AND GROUP VELOCITY MEASUREMENT

We analyse vertical component seismograms of 282 seismic stations across South America (Fig. 2). The seismograms were recorded by stations from permanent networks: RSBR (Rede Sismográfica Brasileira); OS (Observatório Sismológico - UnB); C1 (Red Sismológica Nacional); EC (Ecuador Seismic Network); IU (Global Seismograph Network); GT (Global Telemetered Seismograph Network); CU (Caribbean USGS Network); G (GEOSCOP); CM (Red Sismológica Nacional de Colombia); II (IRIS/IDA Seismic Network); WC (Curacao Seismic Network) and WA (West Central Argentina Network), and from temporary networks: XC (Pantanal, Chaco and Paraná structural studies, 2016–present); XT (Caribbean Passive Experiment, 2003–2005) and ZG (Central Andean Uplift and the Geodynamics of the High Topography, 2010–2012). We measure Rayleigh wave group velocities using the single station method, selecting 1043 earthquakes from the United States Geological Survey (USGS) bulletin for the period from 2002 to 2019, with a magnitude $M_w \geq 5$ and a focal depth $z \leq 100$ km, for source–receiver distances between 15° and 65°, to avoid complications from near-source effects and interference from higher modes, and to achieve a better signal-to-noise ratio. Most of the selected events are distributed along the Andean Orogenic Belt (Fig. 3a) and have magnitudes between 5.0 and 6.0 M_w (Fig. 3c). Thus, our data set tends to have paths of a relatively small length, with most of the source–receiver distances between 25° and 35° (Fig. 3b). The period range of each dispersion curve varies according to the path, depending on earthquake magnitude and source–receiver distance. As a consequence, periods are unevenly sampled (Fig. 3d).

All seismograms were visually examined to discard waveforms with excessive noise and instrument artefacts. Prior to group velocity measurement, we apply pre-processing steps to each seismogram. We remove the mean and linear trend, apply a time-domain cosine taper, deconvolve the instrument response from the seismogram, and bandpass the signal. Also, a phase-matched filter (Herrin & Goforth 1977) is applied to isolate the fundamental mode Rayleigh wave, removing higher modes. To measure group velocity, we use the multiple filter analysis technique (Dziewonski *et al.* 1969) using the Computer Programs in Seismology routines of Herrmann (2013). The approach implemented in this package minimizes a systematic error in group velocity measurement of individual recordings (Shapiro & Singh 1999). After the described procedure, we obtain a total of 17 838 paths, covering most of the South American continent. The number of dispersion measurements reaches its maximum at the period of 30 s and decreases for both shorter and longer periods (Fig. 3d). This decrease at shorter periods is related to shallow velocity heterogeneity, which makes the signal more complex, and at longer periods is associated with the energy released by low magnitude earthquakes, which are not able to excite Rayleigh waves to generate high signal-to-noise ratios for appropriate measurements. We only retain measurements in the period range of 10–150 s to produce our 2-D Rayleigh wave group velocity maps.

Fig. 4 shows vertical component waveforms sorted by epicentral distances of five stations from the RSBR network (RCLB, PTET, ALF01, JANB and NBLA), which recorded the 7.6 M_w magnitude southern Chile event 122516A (2016 December 25, 14:22:27) from the Global CMT catalogue. The grey waveforms are pre-processed seismograms as described above, and the blue ones are the isolated fundamental mode seismograms after the application of the phase-matched filter. Although the seismograms are records of the same event, they present a quite different pattern among them, revealing a heterogeneous *S*-wave velocity structure beneath the South American continent. Fig. 5 presents group velocity dispersion curves in blue measured from the waveforms in Fig. 4. For comparison, we plotted each curve with standard deviation dispersion curves in grey dashed lines, calculated from the average dispersion of all 17 838 measured curves in this study, which are shown in Fig. 5(f) as a probability density distribution of all Rayleigh wave group velocity dispersion curves. The five dispersion curves lie within the range of one standard deviation from the mean curve, in black, plotted in Fig. 5(f). The dispersion curve obtained at the station PTET (red triangle in Fig. 6a) only presents measurements for periods above ∼25 s most likely due to noise amplification caused by soft quaternary sediments of the Pantanal basin (Assine *et al.* 2015) on shorter periods. Fig. 6 illustrates all dispersion curves measured at each of the five stations shown in Figs 4 and 5. In Fig. 6(a), we have the location of these stations on the topography/bathymetry map of South America, along with the epicentre of all events recorded by them. Figs 6(b)–(f) present the probability density distribution of Rayleigh wave group velocity dispersion curves for each station. Among these five stations, JANB was the one that provided the most dispersion curves to the experiment, with 359 measurements. Then, RCLB contributed with 288 curves, ALF01 with 281, NBLA with 257 and PTET with 67. The average dispersion curves in black show group velocities varying from 2.9 km s^{-1}, at 10 s, to 3.8 km s^{-1}, at 150 s, with a peak of about 3.9 km s^{-1}, at 80 s. The standard deviation curves in grey dashed lines are closer to the average ones on shorter periods, yet overall they are not far from the mean curves by more than 5 per cent.

3 GROUP VELOCITY MAPS

3.1 Tomography method

We use the Fast Marching Surface Tomography (FMST) package (Rawlinson 2005) to estimate the group velocity maps. In the first step, the velocity structure beneath South America is represented by a grid of velocity nodes, with a bi-cubic B-spline interpolation function associated. An optimum balance between recovery, resolution, and computational processing time was found for a grid spacing of 1° × 1°. FMST iteratively solves the forward and inverse steps in order to account for the non-linearity between traveltime and velocity (Rawlinson & Sambridge 2005). Rather than using a conventional ray-tracing method, the forward problem is solved by tracking the entire wave front through the Fast Marching Method (FMM, Sethian 1996; Sethian & Popovici 1999; Rawlinson & Sambridge 2004b). FMM is a grid-based numerical method that solves the eikonal equation via finite differences. The main advantages of FMM over traditional ray tracing methods include avoiding great circle assumptions, finding diffractions in shadow zones and solving wave propagation, even in highly heterogeneous media (see Sethian & Popovici 1999; Rawlinson & Sambridge 2004a).

The inverse step is cast as an optimization problem, where the following objective function $S(\mathbf{m})$ is to be minimized (e.g.

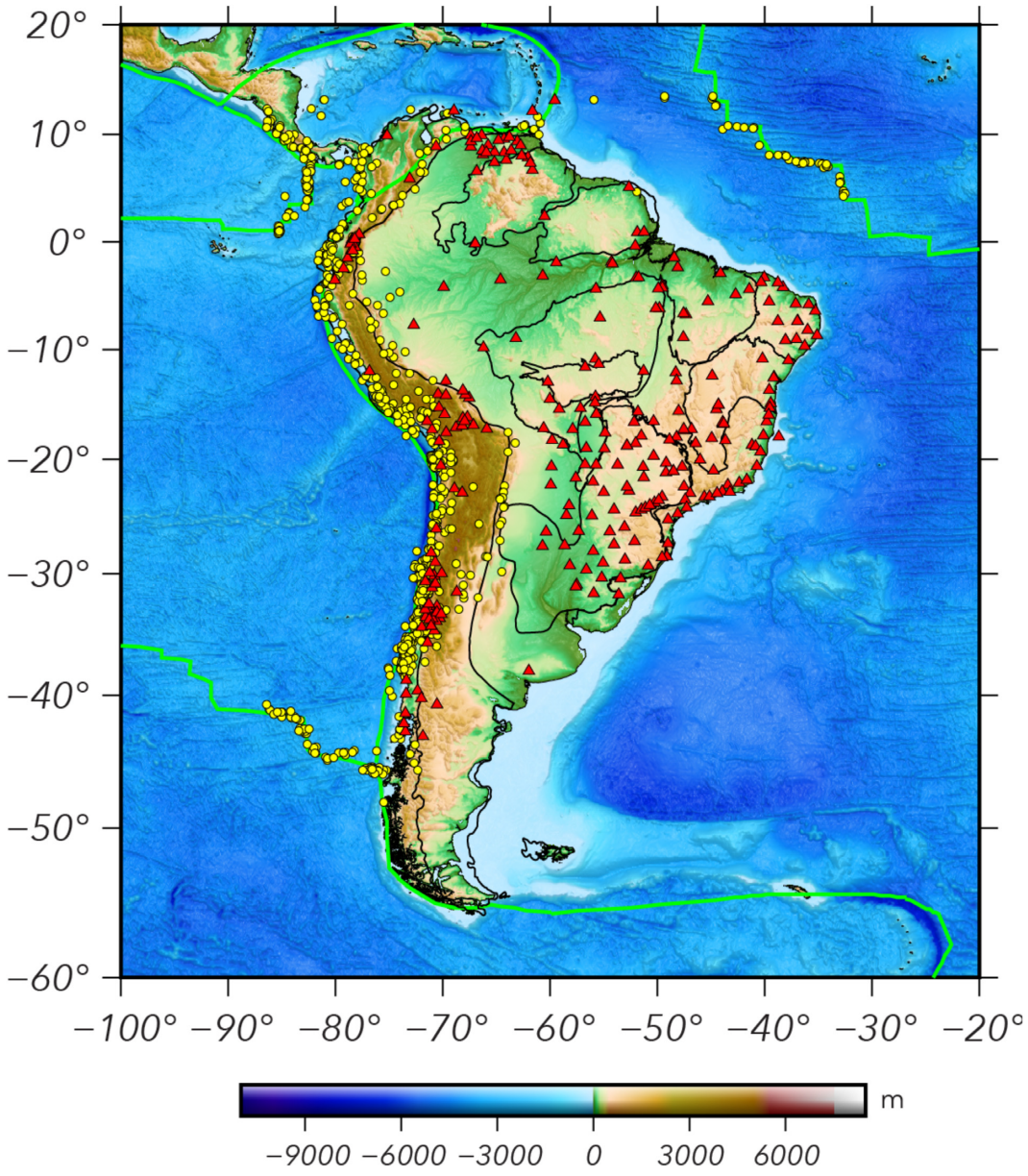

Figure 2. Topography and bathymetry map from ETOPO1 model (Amante & Eakins 2009) with the distribution of stations (red triangles) and earthquakes (yellow circles) across South America. The total number of stations used in this work is 282. We select a total of 1043 earthquakes with magnitude $M_w \geq 5$ and focal depth $z \leq 100$ km from the United States Geological Survey (USGS) bulletin for the period from 2002 to 2019. Black contour represents the main tectonic provinces of South America, as shown in Fig. 1. The green line represents plate boundaries.

Rawlinson *et al.* 2006):

$$S(\mathbf{m}) = (\mathbf{g}(\mathbf{m}) - \mathbf{d}_{obs})^T \mathbf{C}_d^{-1} (\mathbf{g}(\mathbf{m}) - \mathbf{d}_{obs}) + \epsilon(\mathbf{m} - \mathbf{m}_0)^T \mathbf{C}_m^{-1} (\mathbf{m} - \mathbf{m}_0) + \eta \mathbf{m}^T \mathbf{D}^T \mathbf{D}\mathbf{m}, \quad (1)$$

where $\mathbf{m}$ is the model parameters vector, $\mathbf{d}_{obs}$ are the observed traveltime data, $\mathbf{g}(\mathbf{m})$ is the forward operator, which provides predicted data for the forward step, $\mathbf{C}_d^{-1}$ is the inverse data covariance matrix, $\mathbf{m}_0$ is the reference model, $\mathbf{C}_m^{-1}$ is the inverse model covariance matrix, $\mathbf{D}$ is a smoothing matrix operator, ϵ and η are the damping and smoothing coefficients, respectively. The first term on the right-hand side of eq. (1) measures the misfit between observed and theoretical traveltimes. As the solution may not be well constrained by the data alone, regularization terms are added to the objective function. The second term on the right-hand side favours solution models $\mathbf{m}$ that are close to a reference model $\mathbf{m}_0$, and the third one favours smooth models over rough ones. Group velocity values for each period are taken from the 1-D wave speed model for Earth AK135 (Kennett *et al.* 1995) and used as the reference model for the inversion. We assume that the errors in the dispersion measurements are statistically independent and that diagonal elements of the data covariance matrix, $\mathbf{C}_d$, have a constant value of 100 s^2, and the diagonal elements of the model covariance matrix, $\mathbf{C}_m$, have a constant value of 0.09 $km^2\ s^{-2}$.

To find the minimum of eq. (1), we apply the subspace method (e.g. Kennett *et al.* 1988; Sambridge 1990), which is a gradient-based inversion scheme that assumes a local quadratic approximation on the current model. To reduce the computational expense of the inversion, the subspace method projects and minimizes, at each iteration, the quadratic approximation in an n-dimensional subspace

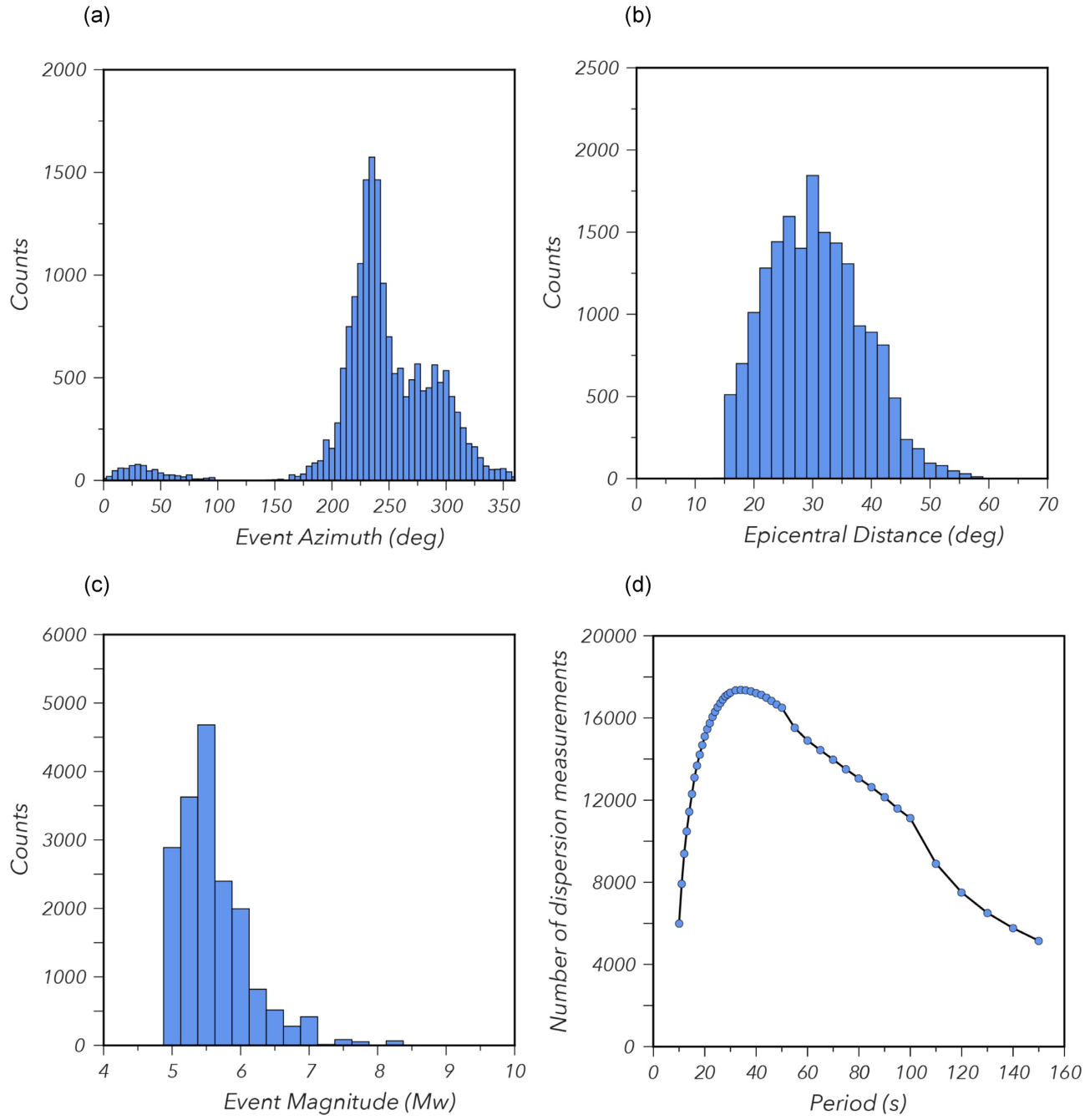

Figure 3. (a) Histogram showing the azimuthal distribution of events recorded by 282 stations in South America (see Fig. 2). (b) Histogram showing the epicentral distance distribution of events recorded by seismic stations within the study area. (c) Histogram exhibiting the earthquake magnitude range of events selected in this study. (d) Number of dispersion measurements as a function of period.

of the model space. For the penalty function of eq. (1), the model perturbation is given by (e.g. Rawlinson *et al.* 2006):

$$\delta \mathbf{m} = -\mathbf{A}(\mathbf{A}^T(\mathbf{G}^T\mathbf{C}_d^{-1}\mathbf{G} + \epsilon\mathbf{C}_m^{-1} + \eta\mathbf{D}^T\mathbf{D})\mathbf{A})^{-1}\mathbf{A}^T\hat{\boldsymbol{\gamma}}, \quad (2)$$

where $\mathbf{A}$ is a projection matrix, $\mathbf{G}$ is the Fréchet derivatives matrix, and $\hat{\boldsymbol{\gamma}}$ is the gradient vector. We do not include event relocation during our inversion procedure, but we expect that data redundancy may average and consequently reduce errors from the dispersion curves.

We analyse the trade-off between satisfying the data and model complexity by inverting the observed data with different sets of damping and smoothing coefficients. To select appropriate values for ϵ and η, we use the L-curve analyses (e.g. Rawlinson *et al.* 2006; Aster *et al.* 2018). First, we set η to zero and perform several inversions, varying ϵ from 10^{-3} to 10^{3}, and we plot the residual data misfit against the variance of the solution model. Then, the same procedure is applied to pick an optimal value for η, by plotting the residual data misfit against the model roughness. Fig. 7 shows L-curves used to select an optimal value for ϵ and η for the following periods: 10, 20, 40, 50, 70, 100, 120 and 150 s. The best values are circulated in black in Fig. 7. We find that $\eta = 10$ and $\epsilon = 10$ are optimal parameters for these periods, except for the period of 150 s, where $\eta = 1$ and $\epsilon = 1$ are the most appropriate values.

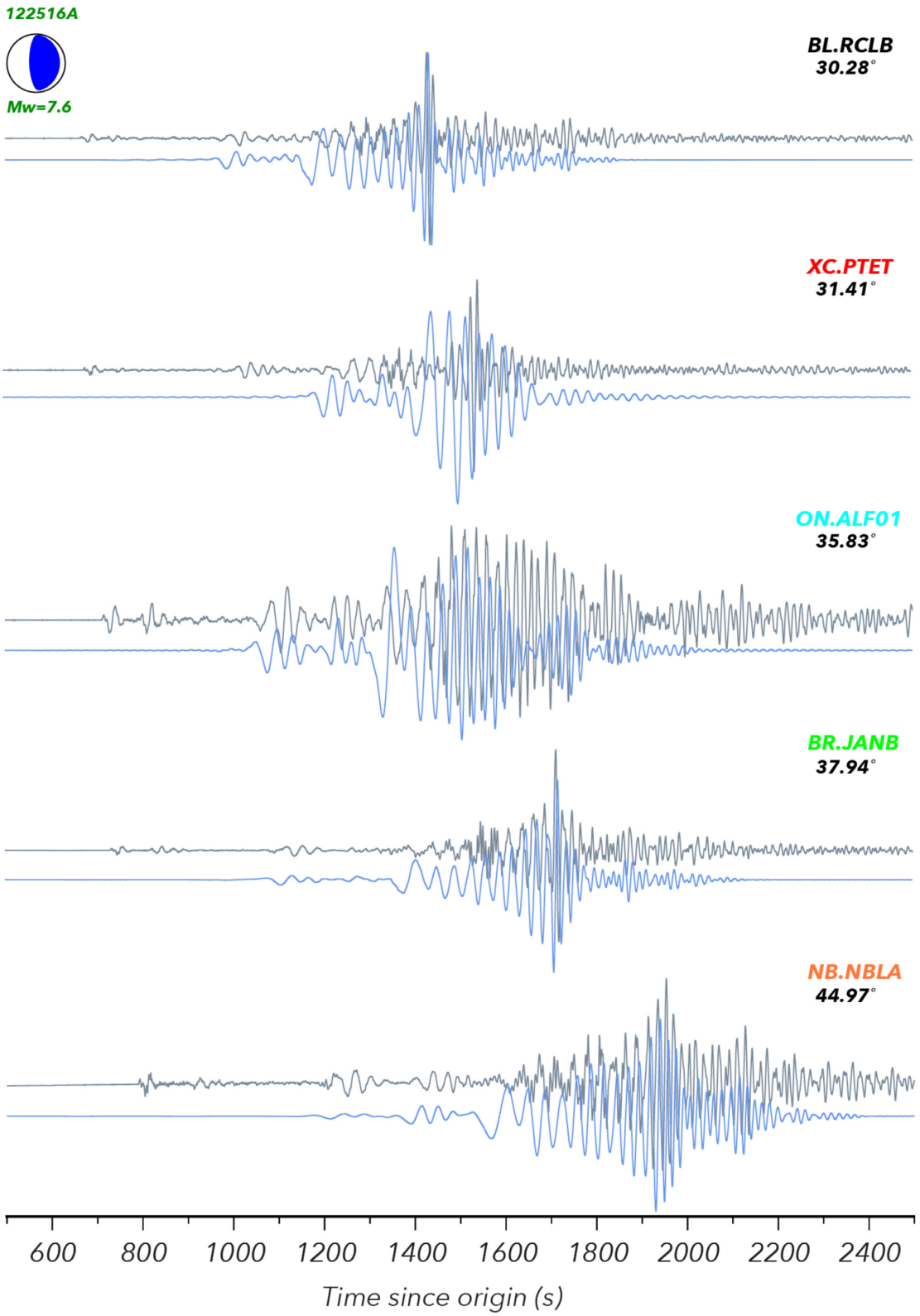

Figure 4. Example of waveforms (in grey) at five RSBR stations (RCLB, PTET, JANB, ALF01 and NBLA), which recorded the southern Chile single event 122516A (2016 December 25 14:22:27) of magnitude 7.6 M_w from the global CMT catalogue. Blue waveforms are the isolated fundamental mode ones. Fig. 6(a) shows the locations of these five stations.

Fig. 8 presents histograms with the traveltime residuals before (blue bins) and after (green bins) inversion at periods of 10, 20, 40, 50, 70, 100, 120 and 150 s. After 10 iterations, for the previously mentioned periods, we observe a traveltime residual reduction of 58, 71, 62, 55, 43, 25, 26 and 20 per cent, respectively. As lateral variations of group velocity amplitudes are smaller at longer periods, then less signal needs to be fitted and traveltime residual reduction is decreased when compared to those obtained at shorter

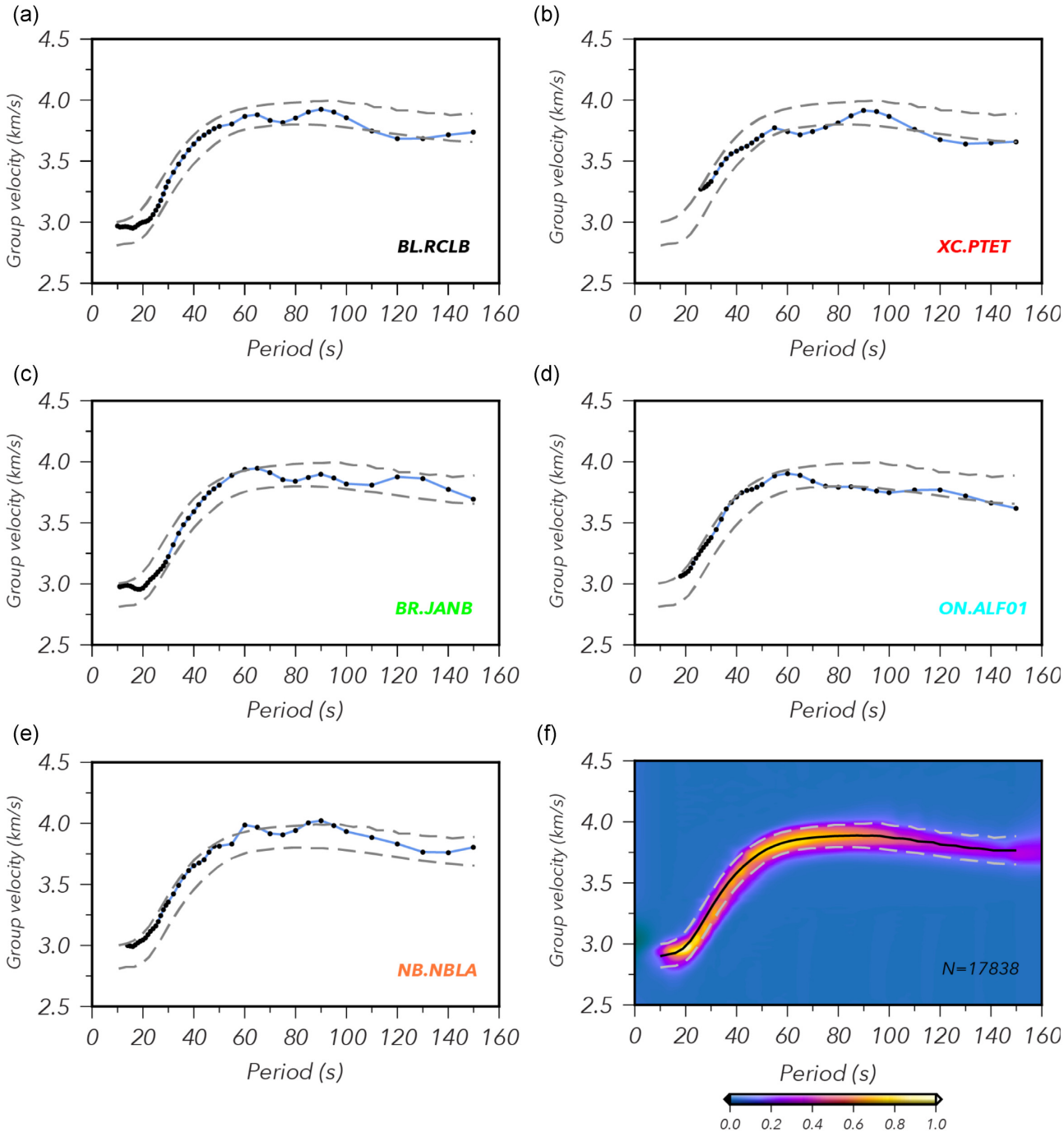

Figure 5. (a)–(e) Blue curves with dots represent group velocity dispersion measurements obtained from the seismograms of Fig. 4, and grey dashed lines are standard deviation dispersion curves calculated from the average dispersion of all 17 838 measured curves in this study. (f) Probability density distribution of all Rayleigh wave group velocity dispersion curves. The black and grey dashed lines are the average and standard deviation curves of all measured dispersion, respectively. The location of stations RCLB, PTET, ALF01, JANB and NBLA can be seen in Fig. 6(a).

periods. Also, traveltime residuals are better adjusted for shorter periods due to larger errors and uncertainties associated with longer periods. The initial traveltime residuals can be as large as 150 s for shorter periods, but they are smaller for longer ones. For the period of 20 s, for example, the initial traveltime residual average is -2.51 s, with a standard deviation of 37.94 s. After the inversion, the final traveltime residual average is reduced to 0.25 s, with a standard deviation of 10.89 s. For the period of 100 s, the initial traveltime residual average is 0.13 s, with a standard deviation of 21.81s. The final traveltime residual average is 0.25 s, with a reduced standard deviation of 16.42 s.

3.2 Checkerboard resolution tests

To qualitatively assess the lateral resolution of our tomography maps, we perform several variants of the checkerboard test in

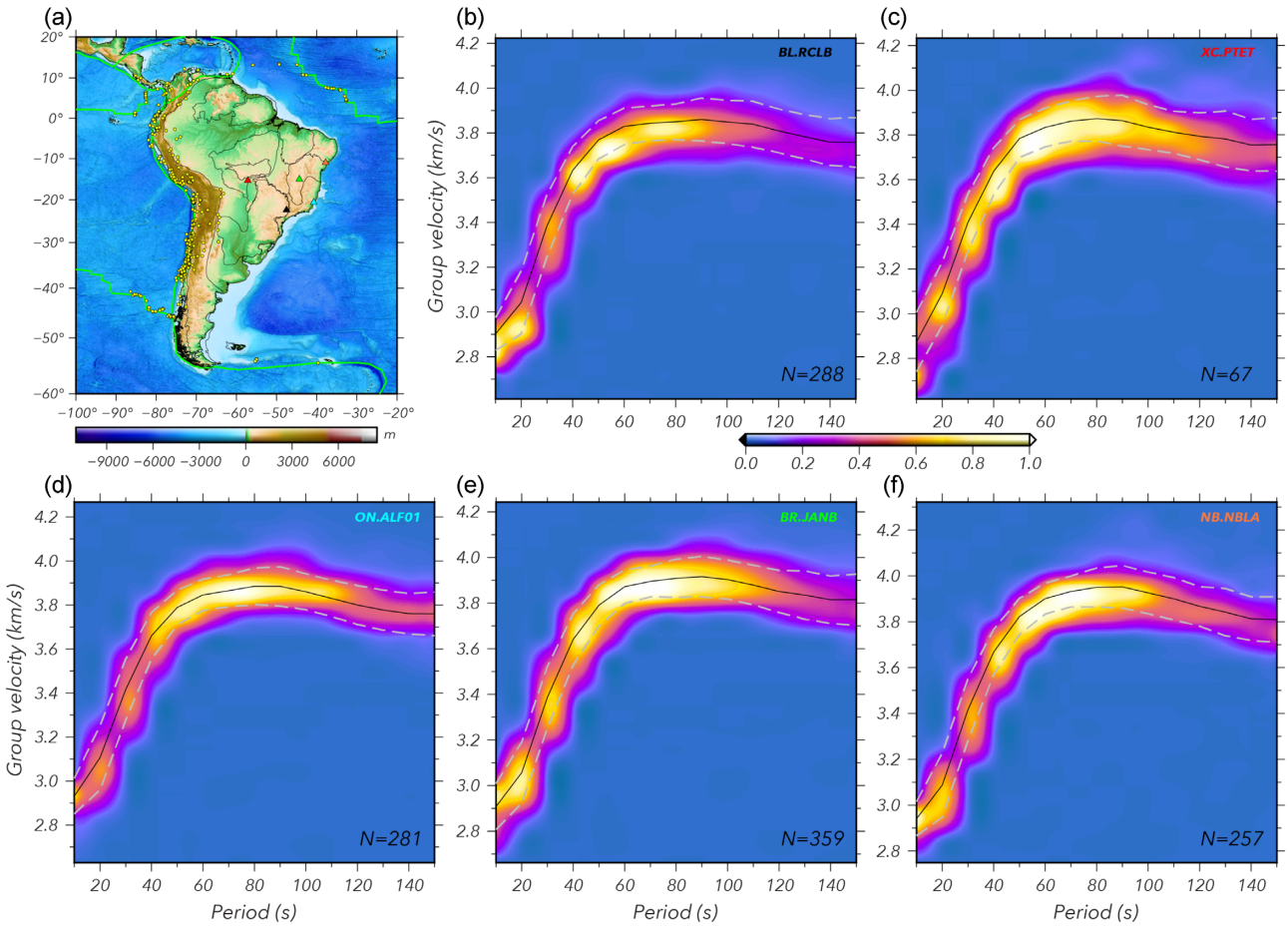

Figure 6. (a) Topography and bathymetry map with the location of the following RSBR network stations: RCLB (black triangle), PTET (red triangle), ALF01 (cyan triangle), JANB (green triangle) and NBLA (orange triangle). The yellow circles depict the epicentre of recorded earthquakes across South America by these five stations. (b)–(f) Probability density distribution of Rayleigh wave group velocity dispersion curves measured for each station. The black line and grey dashed lines are the average and standard deviation curves of measured dispersion, respectively. *N* stands for the number of measured dispersion curves.

which there is a space between alternating high and low-velocity anomalies. This procedure can be thought of as a combination of checkerboard and spike tests. As pointed out by Lévêque *et al.* (1993) and Rawlinson & Spakman (2016), checkerboard results can be misleading and should be interpreted with caution, because small-scale structures may be well retrieved by the test, while long-wavelength structures may be poorly resolved. However, this problem is mitigated by performing several tests varying the anomaly size, and checkerboard tests are still widely used (e.g. Rawlinson *et al.* 2011; Fang *et al.* 2016), providing useful insights on model resolution. Thus, we generate a synthetic data set through an alternating pattern of high and low-velocity anomalies, using the same source–receiver distribution of our observed data set. Group velocity perturbations of –0.8 and 0.8 km s^{-1} are chosen for all tests we perform and they are added to group velocity values from the AK135 model at the period of interest. To simulate sources of error (e.g. mislocation of events, noise, etc.) present in the observed data, a Gaussian noise component is added to each path, with a standard deviation of 6 s. The inversion of this synthetic data set with the subspace method is then carried out, using the same parameters (i.e. grid spacing, damping and smoothing parameters, etc.) as the ones used for the inversion of the observed data. Fig. 9 presents the results of the checkerboard tests for periods of 10, 20, 40, 50, 70, 100, 120 and 150 s, with alternating anomaly patterns of 2° × 2°, 3° × 3°, 4° × 4° and 5° × 5°, respectively. In general, the velocity anomalies are well recovered in the tests, but decreased amplitude is observed in all retrieved models, most likely because of the smoothing and damping regularization parameters used in the inversion. Thus, it is likely that the amplitude of our Rayleigh group velocity maps is also underestimated. Smearing effects are also present, chiefly in regions of uneven azimuthal coverage (see Figs 2 and 3a), such as southern Argentina, especially in the Patagonian block.

3.3 Group velocity maps at periods of 10–150s

In this subsection, we present 2-D Rayleigh wave group velocity maps for periods of 10, 20, 40, 50, 70, 100, 120 and 150 s (Figs 10a–h). Fast group velocities are represented by blue colours and slow group velocities are represented by red colours. As the oceanic areas are poorly sampled in this study, we decide to mask them in our group velocity maps to avoid misinterpretation, discussing only the group velocity contribution to the imaging of the heterogeneous structure beneath the onshore area of South America. Figs 10(a)–(h) show that the slowest group velocity values are

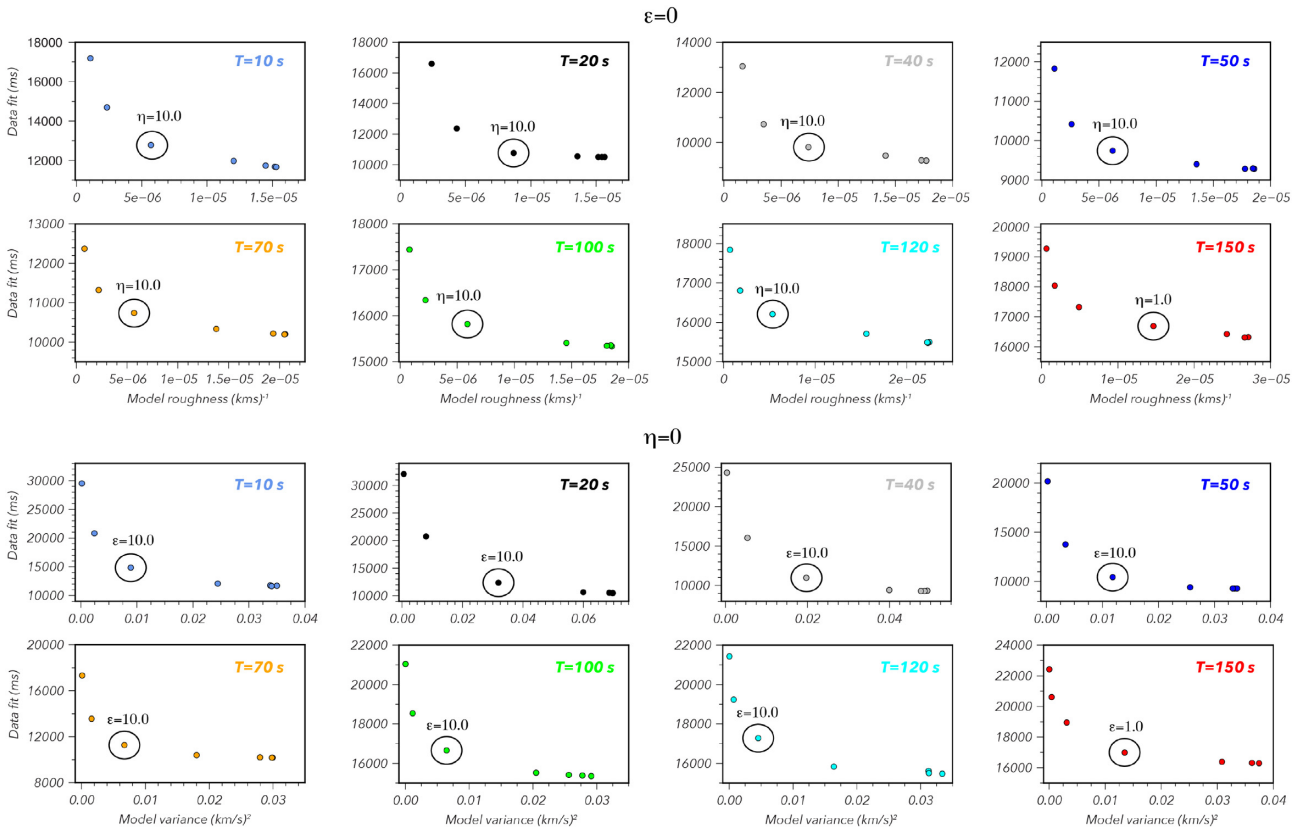

Figure 7. L-curve scheme used to determine optimum values for damping and smoothing parameters for each group velocity map at the periods of 10, 20, 40, 50, 70, 100, 120 and 150 s. In the top panel, we fix $\epsilon = 0$ and vary η from 10^{-3} to 10^{3}, plotting the residual data misfit (along the y-axis) versus the roughness of the solution model (along the x-axis). In the bottom panel, we fix $\eta = 0$ and vary ϵ from 10^{-3} to 10^{3}, plotting the residual data misfit (along the y-axis) versus the model variance (along the x-axis). The selected optimum values for the inversion are circulated in black.

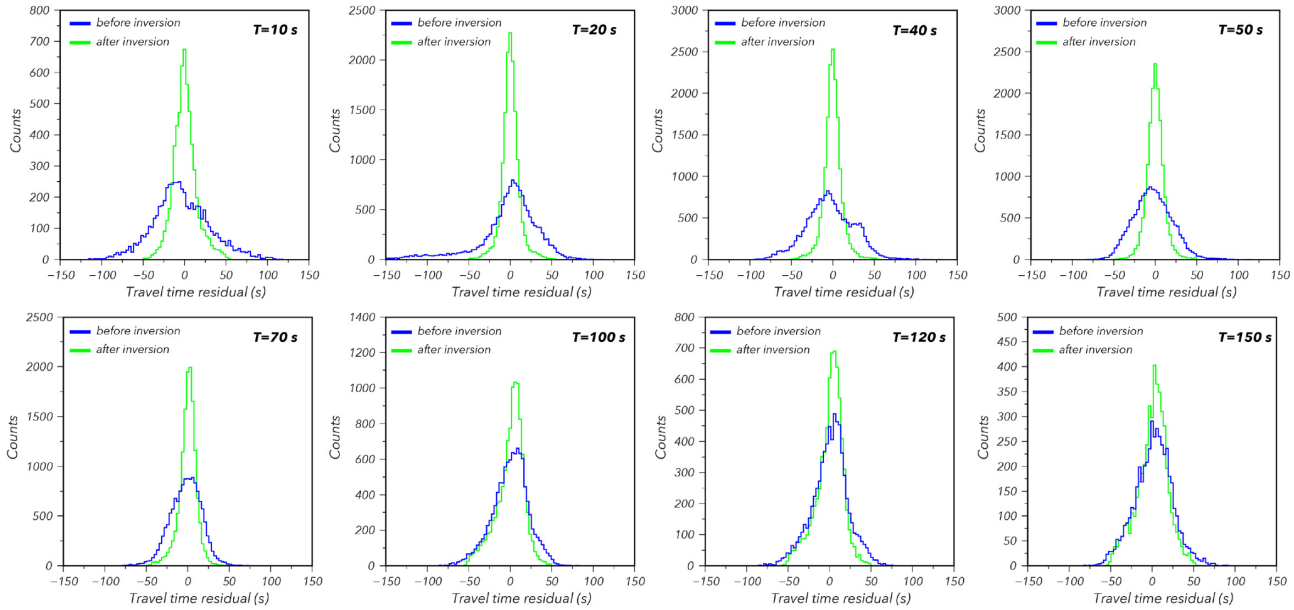

Figure 8. Histograms showing traveltime residuals before (blue bins) and after (green bins) inversion at periods of 10, 20, 40, 50, 70, 100, 120 and 150 s.

mainly concentrated along the Andean Orogenic Belt and can reach group velocity perturbations as low as –20 per cent, as in Fig. 10(a), compared to the reference model AK135 (U_{AK135}). High group velocity perturbations are observed along the Brazilian continental margin and beneath continental roots as the SFC and AmC cratons, with values that can reach up to 8 per cent.

Since the depth of the velocity structure imaged by surface waves depends on the wave period, each group velocity map is able to

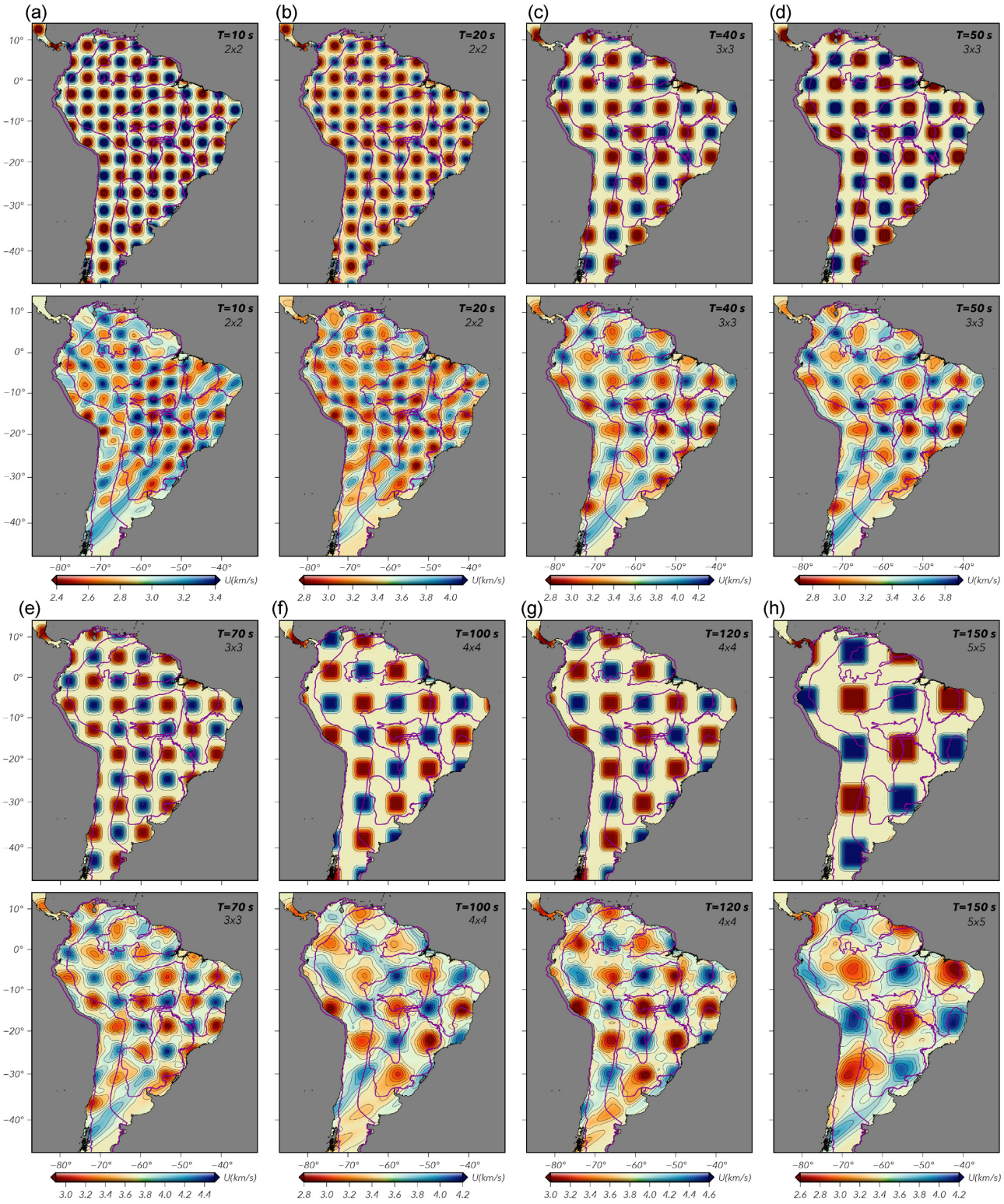

Figure 9. Checkerboard resolution tests of our Rayleigh wave group velocity maps. All maps present group velocity perturbations of –0.8 and 0.8 km s^{-1} added to group velocity values from the AK135 model at the period of interest. Panels (a) and (b) input models with perturbed cell sizes of 2° × 2° and recovered models at periods of 10 and 20 s. Panels (c), (d) and (e) input models with perturbed cell sizes of 3° × 3° and recovered models at periods of 40, 50, and 70 s. Panels (f) and (g) input models with perturbed cell sizes of 4° × 4° and recovered models at periods of 100 s and 120 s. Panel (h) input model with perturbed cell sizes of 5° × 5° and the recovered model at the period of 150 s.

constrain crustal and upper mantle heterogeneities caused by composition and temperature variations at different depths. Therefore, to inspect our tomographic images at different depths, we plot the sensitivity kernels of Rayleigh wave group velocities to shear-wave velocities at different periods, as illustrated in Fig. 10(i). The sensitivity kernels are calculated using the AK135 model. As Fig. 10(i) shows, for Rayleigh wave group velocities, there is approximately a one-to-one relationship between period and depth, that is, the

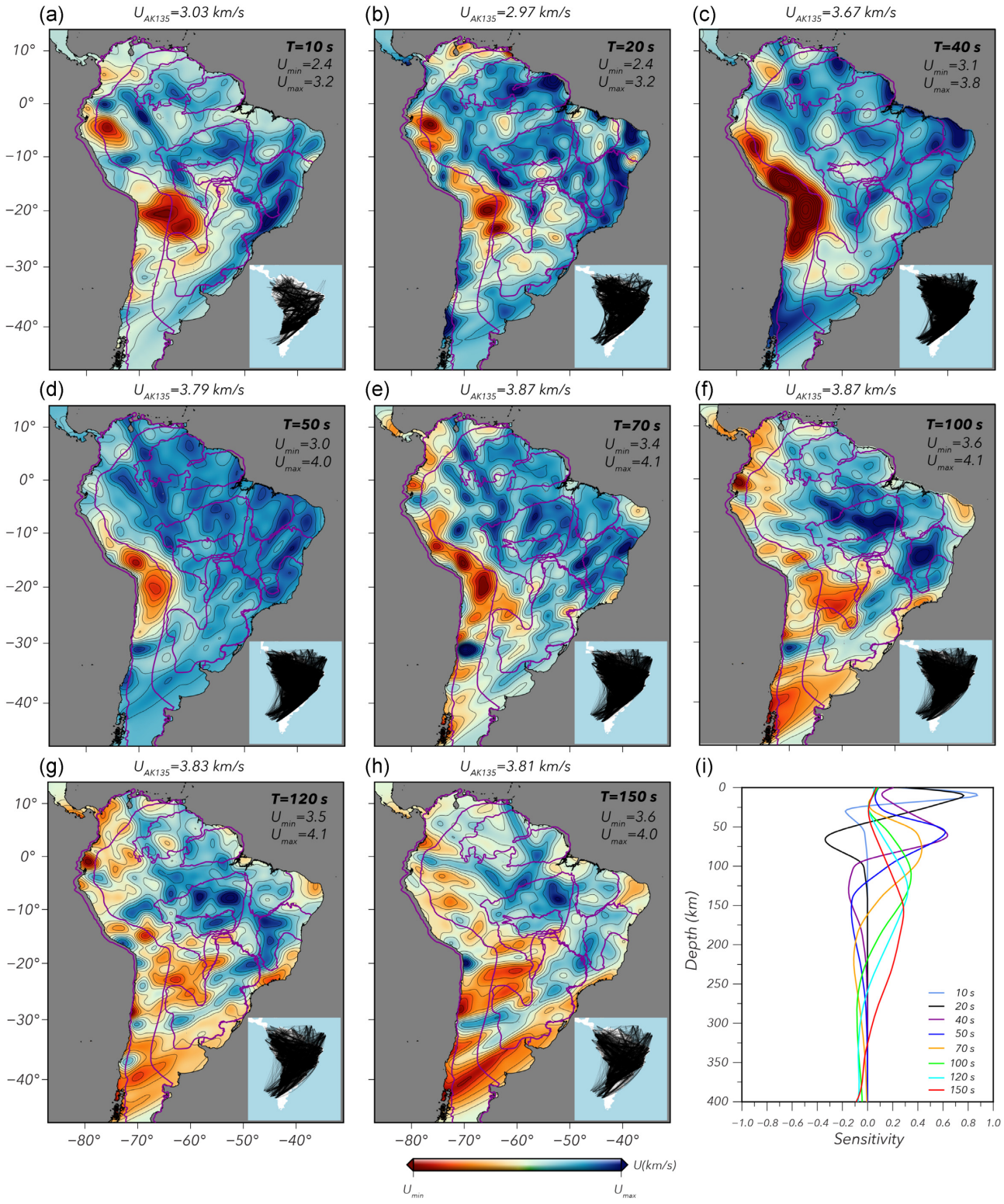

Figure 10. South America Rayleigh wave group velocity maps at periods of (a) 10 s, (b) 20 s, (c) 40 s, (d) 50 s, (e) 70 s, (f) 100 s, (g) 120 s and (h) 150 s. The ray path coverage of each map is represented in the right-hand bottom corner of each panel. Blue colours represent fast group velocities and red colours indicate slow group velocities. Purple contours are the tectonic provinces illustrated in Fig. 1. On each map, $U_{\min}$ and $U_{\max}$ stand for minimum and maximum group velocities, respectively, and U_{AK135} represents the reference velocity from the AK135 model at the period of interest. (i) Sensitivity kernels of Rayleigh waves to shear-velocity derived from the AK135 velocity model for the periods in (a)–(h).

sensitivity peak for the period of 10 s is at a depth of about 10 km, while the sensitivity peak for the period of 150 s is at a depth of about 150 km. From the sensitivity kernel, we can infer that Rayleigh wave group velocities at periods of 10 and 20 s are mostly sensitive to shallow structure, such as basins, exposed basement and upper and middle crust. As the period increases, surface waves are more affected by deeper *S*-wave velocity variations. Thus, group velocity maps of 40 and 50 s are mainly sensitive to the shear-velocity

structure in the lower crust and uppermost mantle. At the periods of 70, 100, 120 and 150 s, the group velocity maps are influenced by lithospheric heterogeneities from about 70 to 150 km depth.

4 DISCUSSION

4.1 Comparison with previous Rayleigh wave group velocity studies

Compared to previous group velocity studies for South America (e.g. Vdovin *et al.* 1999; Feng *et al.* 2004; Rosa *et al.* 2016b), our models present better resolution, mainly for the maps at shorter periods. The imaged long-wavelength heterogeneities exhibit a reasonable agreement among all maps. For example, a prominent elongated slow group velocity feature, found along nearly the entire western edge of South America, following the Andes on our maps of 40 and 50 s, is also observed in the models derived by Vdovin *et al.* (1999), Feng *et al.* (2004) and Rosa *et al.* (2016b). This feature is probably related to the thick crust in the Andean region, which may reach values of 70 km (e.g. Rivadeneyra-Vera *et al.* 2019), and clearly separates the South American Platform from the Andean fold belt. The image of large cratonic areas as the SFC and AmC is also present in our study and in the previous ones, although the division of the AmC into the Guyana and Guaporé shields is not resolved by the model of Vdovin *et al.* (1999).

Small-scale structures, as the Pantanal, Tucano-Jatobá, Alto-Tapajós sedimentary basins and the São Luís, Rio Apa, Rio Tebicuary and Rio de la Plata cratons, are illuminated in our models, yet they are absent or not well constrained in the previous velocity group maps derived for South America. Interestingly, although the AmC is a structure present in all previously cited group velocity maps, only in our model we identify small-scale heterogeneities that may be linked to the geochronological provinces of this cratonic area (Tassinari & Macambira 1999).

4.2 Short period group velocity maps

Fig. 11(a) presents the sediment thickness map of the South American continent from the CRUST1.0 model (Laske *et al.* 2013), which is a compilation of local and regional basement information, and Fig. 11(b) shows the topography density model (UNB_TopoDens) of Sheng *et al.* (2019), which is based on a global lithology map from geological data. Sediment thickness across South American basins is highly variable, ranging from thin sedimentary layer basins, such as Pantanal and Parecis, where the depth to the basement reaches a few hundred meters (e.g. Ussami *et al.* 1999b; Barros & Assumpção 2011), to thick basins, such as Marajó, where sediment thickness may reach up to 11 km (e.g. Costa *et al.* 2002). Although our 2-D group velocity maps have been derived with no *a priori* geological information constraints, Figs 11(c) and (d) show that they present an excellent agreement with the maps of Figs 11(a) and (b).

Slow group velocities on the maps of 10 and 20 s are better correlated with sedimentary basin thicknesses of Fig. 11(a) (e.g. Paraná, Chaco-Paraná, Parnaíba, Amazon, Solimões, Parecis, Marajó, Madre de Dios, Llanos, Oriente-Marañon, Ucayali, Acre and Chaco-Tarija), and with low topography density values of Fig. 11(b). Our short period maps of Figs 11(c) and (d) also show slow group velocities related to small-scale sedimentary basins such as the Tucano-Jatobá Basin (10°S, 37°W, e.g. Ussami *et al.* 1986; Magnavita *et al.* 1994), Pantanal Basin (18°S, 57°W, e.g. Ussami *et al.* 1999b; Assine *et al.* 2015), Alto-Tapajós Basin (8°S, 58°W, e.g. Toczeck *et al.* 2019) and the Llanos Basin (5°N, 72°W, e.g. Mora *et al.* 2019), in northeastern Colombia. Another interesting small-scale feature present on our map of 10 s is a slow group-velocity coincident with the sedimentary cenozoic cover in the axis of the Paraná River, in the PB (see Rosa *et al.* 2016a). On the other hand, fast group velocities are related to regions of exposed basement and high surface densities, as for some portions of the AmC, SFC, São Luis, Rio de La Plata cratons, and the BP, MP and TP provinces. This is probably caused by a more stable and consolidated character of the crystalline basement rocks compared to the sedimentary ones.

The slowest group velocities from the maps of 10 and 20 s are observed underneath the Oriente-Marañon Basin, Ucayali Basin, Chaco-Tarija Basin (CTB) and Altiplano-Puna Volcanic Complex (APVC). The Oriente-Marañon Basin is a Late Permian-Early Triassic sub-Andean foreland basin between Ecuador and Peru, in western South America (Baby *et al.* 2013; Zamora & Gil 2018), which has a sedimentary thickness as large as 4 km, while the Ordovician Ucayali Basin is located in Peru, with sedimentary fills of up to 5 km (Roddaz *et al.* 2005). The Late-Cenozoic CTB, between Bolivia and Argentina, in the central Andes (Uba *et al.* 2006), has a sedimentary thickness of about 5 km. The APVC is an 11–1 Ma silicic volcanic field, located in the central Andes, which lies above a thick crust of about 70 km (De Silva 1989). Beneath the APVC, using a joint inversion scheme of surface waves dispersion curves and receiver functions, Ward *et al.* (2014) imaged a ∼11-km-thick low-velocity zone (extending from ∼4 to 25 km), which was interpreted as a plutonic complex, sourcing this volcanic system. Such a structure coincides with the location of the slow group velocity of about ∼2.3–2.4 km s^{-1} on our maps.

The fastest group velocities of the map of 10 s are related to the MP, across the Brazilian continental margin, and to the AmC and SFC cratons. The MP is a geological orogenic province formed by a mosaic of distinct Archean, Palaeoproterozoic and Mesoproterozoic terranes, which were deformed during the Neoproterozoic/Early Palaeozoic Brasiliano Orogeny (Silva *et al.* 2005). The AmC is a large cratonic area divided into two Precambrian shields, the Guaporé and Guyana Shields, separated by the Palaeozoic AmB, circumscribed by Palaeoproterozoic and Mesoproterozoic fold belts (Tassinari & Macambira 1999; Cordani *et al.* 2009). The SFC consists of Archean and Palaeoproterozoic cratonic nuclei, in general smaller than the ones found in the AmC, part of the much larger Congo Craton, and bounded by the Neoproterozoic Brasília, Araçuaí, Riacho do Pontal and Sergipano orogenic belts (Almeida *et al.* 1981; Brito Neves & Fuck 2014). Therefore, the increased group velocity values are consistent with these older and relatively stable basement rocks. Also, fast group velocities on the map of 10 s are observed in the upper crust structure beneath Fitzcarrald arch. Located in northern South America, the Fitzcarrald arch is a 4 Ma broad uplift, most likely caused by a ∼5 km crustal thickening in response to the Nazca Ridge flat subduction (Espurt *et al.* 2007; Bishop *et al.* 2018).

On the map of 20 s, the AmC geochronological provinces as the Central Amazonian (>2.6 Ga), Maroni-Itacaiúnas (2.45–1.93 Ga), Ventuari-Tapajós (2.05–1.80 Ga), Rio Negro-Juruena (1.82–1.60 Ga), Sunsás (1.20–0.95 Ga) and the São Luís, Rio Apa, Rio Tebicuary and Rio de la Plata cratons are observed as regions of fast group velocities. The AmC geochronological provinces are made up of Archean, Palaeoproterozoic and Mesoproterozoic crustal segments, which were formed through collision/accretion events (Cordani *et al.* 2009). Located in northern Brazil, the São Luís Craton is

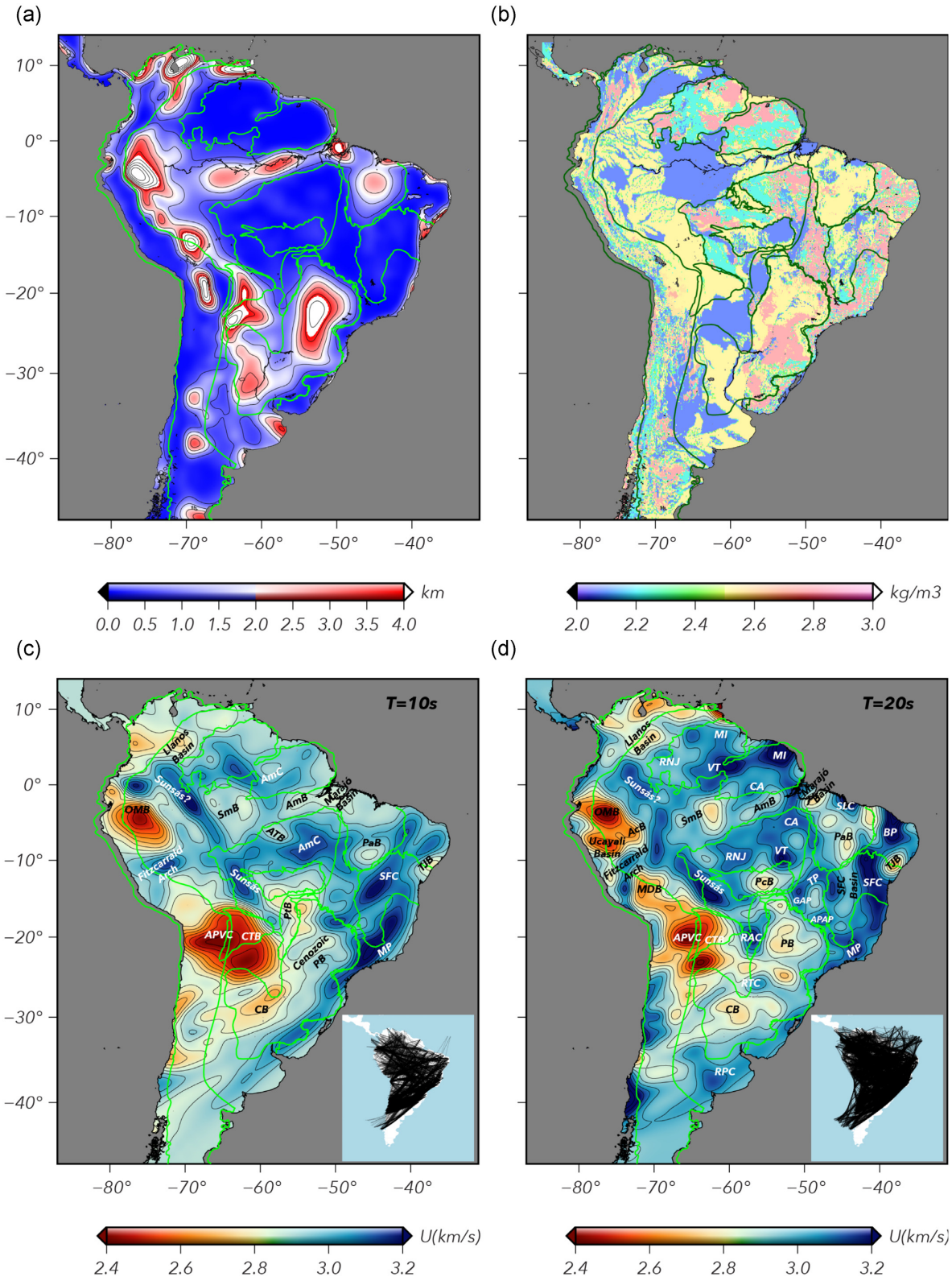

Figure 11. (a) Sedimentary thickness map for South America, obtained from the CRUST1.0 model (Laske *et al.* 2013). (b) Topography density model (UNB_TopoDens) of Sheng *et al.* (2019). Rayleigh wave group velocity maps for periods of (c) 10 s and (d) 20 s. AcB: Acre Basin, APVC: Altiplano-Puna volcanic complex, AmB: Amazon Basin, AmC: Amazonian Craton, APAP: Alto Paranaíba Alkaline Province, ATB: Alto-Tapajós Basin, BP: Borborema Province, CA: Central Amazonian, CB: Chaco-Paraná Basin, CTB: Chaco-Tarija Basin, GAP: Goiás Alkaline Province, MDB: Madre de Díos Basin, MP: Mantiqueira Province, MI: Maroni-Itacaiúnas, OMB: Oriente-Marañon Basin, PB: Paraná Basin, PcB: Parecis Basin, PaB: Parnaíba Basin, RAC: Rio Apa Craton, RPC: Rio de La Plata Craton, RNJ: Rio Negro-Juruena, RTC: Rio Tebicuary Craton, SFC: São Francisco Craton, SLC: São Luís Craton, SmB: Solimões Basin, TJB: Tucano-Jatobá Basin and VT: Ventuari-Tapajós.

composed of Archean and Palaeoproterozoic cratonic fragments of the much larger West African Craton (Klein *et al.* 2005), while the Rio Apa Craton is a Palaeoproterozoic cratonic fragment, formed by accretionary events and encompassed within the Paraguay belt, located between Brazil and Paraguay (e.g. Cordani *et al.* 2010; Teixeira *et al.* 2020). Although dated by Cordani *et al.* (2001), from U-Pb geochronology analysis, with an age of about 2.0 Ga, the basement rocks of the Rio Tebicuary complex were only interpreted as a thin cratonic crust after the gravity data modelling performed by Dragone *et al.* (2017). Our results show the presence of a small fast velocity structure that coincides with the location of the Rio Tebicuary Craton, possibly corroborating its existence. Along the northern border of the PB, our map at a period of 20 s shows two fast velocity structures that coincide with the location of the Goiás (GAP) and Alto Paranaíba (APAP) Alkaline Provinces. The GAP (Brod *et al.* 2005) and APAP (Gomes & Comin-Chiaramonti 2005) are two large kamafugite provinces associated with an extensive Late Cretaceous alkaline magmatism, which took place along the 125AZ lineament. Gravity and magnetic studies in these provinces (e.g. Dutra *et al.* 2012; Mantovani *et al.* 2016) show that alkaline intrusions can reach up to 18 km in depth, as in the GAP, and are denser ($>$2900 kg m^{-3}) than the surrounding upper crust. Thus, denser rocks at shallower depths could explain the faster group velocity underneath the GAP and APAP. The Archean–Palaeoproterozoic Río de la Plata Craton (RPC) is almost entirely covered by a pile of younger sediments, hampering its borders detection, with the main outcrop areas including the crystalline basement in the central to southwestern Uruguay, the Buenos Aires Complex of the Tandilia Belt, in Argentina and the Taquarembó block, in Brazil (Rapela *et al.* 2007; Oyhantçabal *et al.* 2011). Despite the presence of a fast group velocity structure near the Sierra de la Ventana, within the RPC delimitation proposed by Oyhantçabal *et al.* (2011), our ray path coverage is insufficient to properly determine the size and extension of this cratonic segment in southwestern South America, as shown in Figs 9(a) and (b).

4.3 Intermediate period group velocity maps

Because the group velocity maps at 40 and 50 s are sensitive to crustal velocity and thickness, for comparison with our results, in Fig. 12(a) we plot the crustal thickness South American map of Rivadeneyra-Vera *et al.* (2019), which presents a compilation of previous estimated crustal thickness values along with new measurements obtained from receiver functions. The crustal thickness map of South America shows that the thickest crustal values are beneath the central Andres, ranging from 55 to 70 km. Cratonic areas, as an example the AmC and SFC, also present thick crust, with values as large as 42 km. Thin crust is observed along part of the Brazilian continental margin, as for the MP, and underneath the BP, CTB, PtB, AcB and PcB. A receiver function study by Albuquerque *et al.* (2017) found that crustal thickness is highly variable in the AmC, ranging from 27.4 to 48.6 km. This variation is reflected on our group velocity maps of 40 and 50 s as an alternating pattern of fast and slow group velocities along the AmB and SmB, culminating in a transition between fast and slow group velocities in the AcB (see Figs 12c and d), where the reported crustal thickness is around 27 km (Albuquerque *et al.* 2017). For the Ribeira fold belt, within the MP, França & Assumpção (2004) estimated, from receiver functions, a crustal thickness ranging from 34 to 42 km, with a thinning trend towards the coast. The same trend is observed in Fig. 12(a) along the whole MP. This observed crustal thinning can be due to the extensional process related to the break-up of West Gondwanaland. Then, denser mantle material at a shallower depth may explain the fast group velocities on our maps. Previous crustal thickness estimates for the BP (e.g. Pavão *et al.* 2013; Lima *et al.* 2015; Luz *et al.* 2015; Fianco *et al.* 2019) reveal a thin crust, with Moho depth varying from 30 to 40 km, which could be associated with crustal delamination or stretching. This thin crust is imaged on our 40 and 50 s maps as a fast group velocity, thus corroborating previous results. For the PcB, the study by Albuquerque *et al.* (2017) indicates a thin crust of about 30 km, located in the central-northern portion of the basin, neighboured by a thick crust ($>$47 km) towards the AmC. In this region, we observe a slow group velocity in contrast to the fast velocity found in other regions of crustal thinning.

Beneath the PB and CB, the slow group velocities on the map of 40 s are in agreement with those derived by Shirzad *et al.* (2019), from ambient seismic noise tomography at the same period, and they still correlate with the map of the sedimentary thickness of Fig. 11(a), albeit we expected this period to be mainly influenced by the velocity structure of the lower crust, as shown by the sensitivity kernels of Rayleigh waves to shear-velocity in Fig. 10(i). A normal to thick crust varying from 40 to 45 km (e.g. Julià *et al.* 2008; Rivadeneyra-Vera *et al.* 2019) is observed beneath the PB and a thin to normal one, ranging from 35 to 40 km (e.g. Rosa *et al.* 2016b; Rivadeneyra-Vera *et al.* 2019), is detected beneath the CB. Thus, the observed slow group velocity underneath these two basins may not necessarily be due to the effect of the sediment structure above the basement, yet due to the flexural load imposed by the sedimentary package that bends the slower shallow crustal material to greater depths. Slow group velocities correlating with normal to thick crust are also observed beneath the AmB, SmB and PaB. Albuquerque *et al.* (2017) found values of around 39 km for the crust beneath the AmB and SmB. From a deep crustal seismic profile, Daly *et al.* (2014) estimated an average value of 40 km for the PaB crustal thickness.

The most striking feature of our map at 40 s is a fast group velocity structure with the same NE trend of the Transbrasiliano lineament (TBL), a Neoproterozoic megashear fault that crosses a large part of the South American continent and extends to Africa (Fairhead & Maus 2003; Santos *et al.* 2008; Cordani *et al.* 2013). To compute a precise model for the Earth's magnetic field, Fairhead & Maus (2003) combined the data set from two-satellite mission, Ørsted and CHAMP, respectively. The model derived by them detected the TBL as a zone of low analytic signal of the magnetic field, most likely due to low susceptibility crust, separating the SFC, to the SE, from the AmC, to the NW. In Fig. 12(b), we can also observe the TBL as positive amplitude magnetic anomaly, in the magnetic anomaly map EMAG2v3 (Earth Magnetic Anomaly Grid) of Meyer *et al.* (2017), which combines data from satellite, ship, and airborne magnetic measurements and has a resolution of 2 arc-minute. The fast group velocity NE trend observed on our map may be because of a crustal thinning along the TBL. However, the receiver functions by Rivadeneyra-Vera *et al.* (2019) do not show a clear crustal change through the TBL as we can see in Fig. 12(a), albeit there are several points of shallower Moho depth and a huge gap of points in the PaB that does not allow us to preclude that the TBL overlies a crustal thinning zone.

4.4 Long period group velocity maps

For comparison with our group velocity maps of 100 and 150 s, we plot in Figs 13(a) and (b) the version 2 of the isotropic global

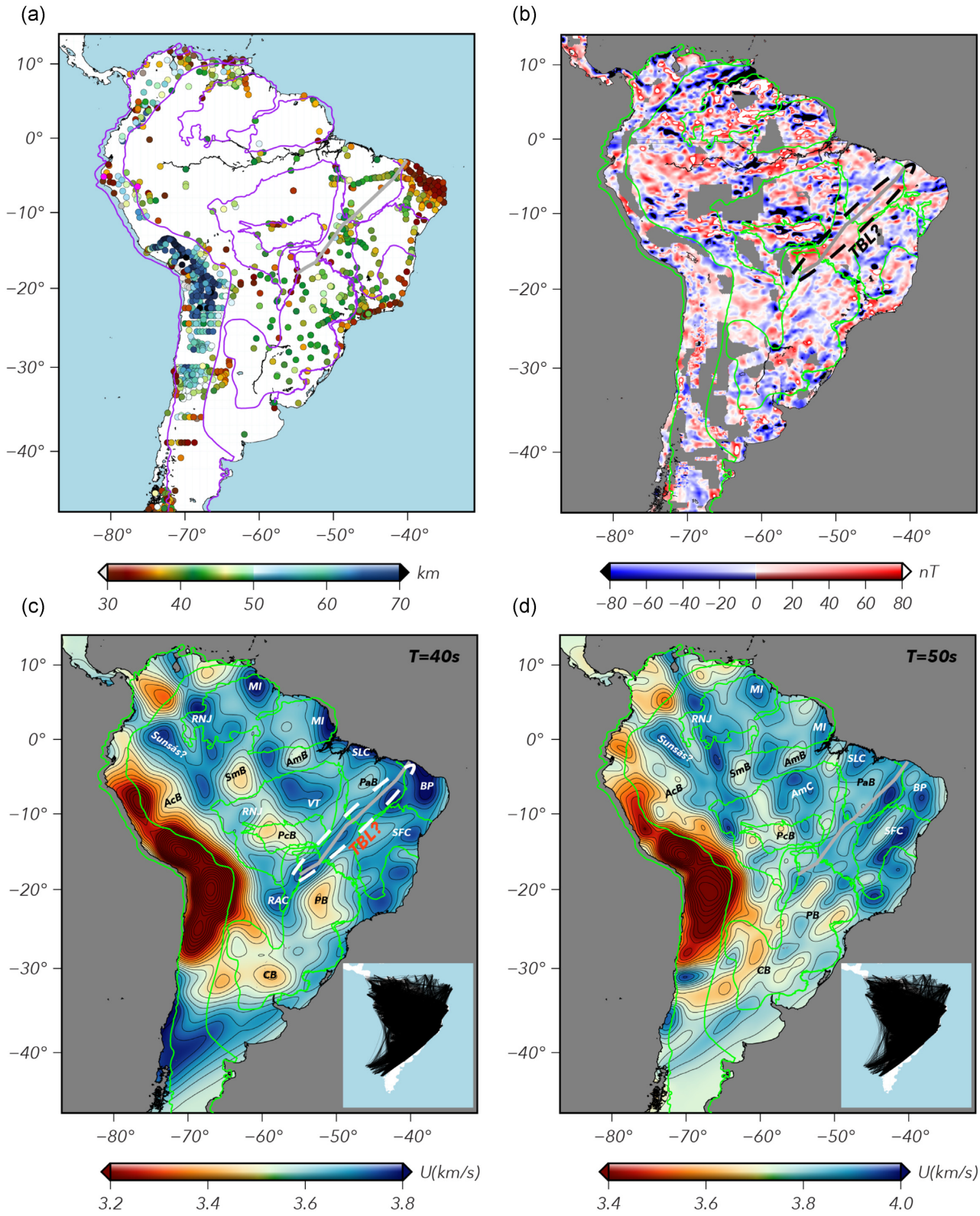

Figure 12. (a) Crustal thickness estimates of the South American continent, obtained from Rivadeneyra-Vera *et al.* (2019). (b) Magnetic anomaly map EMAG2v3 (Earth Magnetic Anomaly Grid) of Meyer *et al.* (2017). Group velocity maps of (c) 40 s and (d) 50 s. The Transbrasiliano Lineament (TBL) is indicated in each figure by a grey line. AmB: Amazon Basin, AmC: Amazonian Craton, BP: Borborema Province, CB: Chaco Paraná Basin, MI: Maroni-Itacaiúnas, PB: Paraná Basin, PcB: Parecis Basin, PaB: Parnaíba Basin, RAC: Rio Apa Craton, RNJ: Rio Negro-Juruena, SFC: São Francisco Craton, SLC: São Luís Craton, SmB: Solimões Basin and VT: Ventuari-Tapajós.

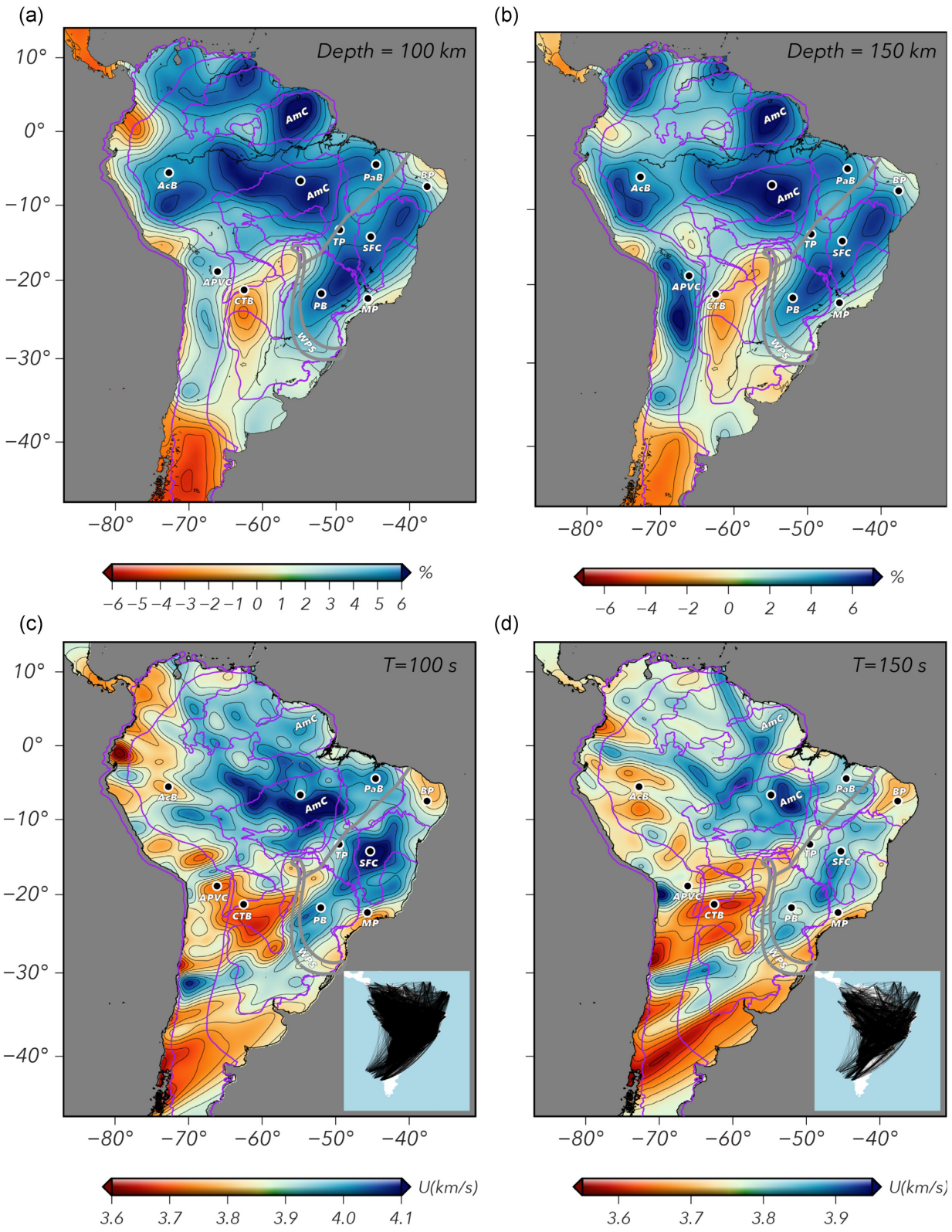

Figure 13. Horizontal slices of the isotropic global *S*-wave velocity model SL2013sv of Schaeffer & Lebedev (2013) at the depths of (a) 100 km and (b) 150 km. Group velocity maps of (c) 100 s and (d) 150 s derived in this study. The Transbrasiliano Lineament (TBL) is indicated in each figure by a grey line. AcB: Acre Basin, AmC: Amazonian Craton, APVC: Altiplano-Puna volcanic complex, BP: Borborema Province, CTB: Chaco-Tarija Basin, MP: Mantiqueira Province Province, PB: Paraná Basin, PaB: Parnaíba Basin, SFC: São Francisco Craton and TP: Tocantins Province. The Western Paraná Suture (WPS) is indicated by a grey contour. The black–white dots indicate the location where 1-D *S*-wave velocity depth profiles were estimated.

S-wave velocity model SL2013sv of Schaeffer & Lebedev (2013) at the depths of 100 and 150 km. These depths approximately coincide with the peak of the highest sensitivity of group velocity to shear-velocity, corresponding to the maps of Figs 13(c) and (d). The SL2013sv is a model derived from a large collection of vertical-component broad-band seismograms using an automated multimode waveform inversion procedure of surface and *S* waves. For a period range from 11 to 450 s, the algorithm extracted a set of linear equations, which were posteriorly inverted for a 3-D model of shear and compressional speeds and azimuthal anisotropy within the crust, upper mantle and transition zone.

Our group velocity maps in Figs 13(c) and (d) present a good correlation with the *S*-wave velocity perturbation model in Figs 13(a) and (b). Fast group velocities are observed beneath the AmC, SFC, PB, PaB, and they match the high *S*-wave velocity perturbations in the SL2013sv model in the same regions. From *S* receiver function analysis, Heit *et al.* (2007) estimated punctual lithosphere–asthenosphere boundary (LAB) depths larger than 120 km for the AmC, SFC and PB, which are most likely related to their deep cratonic roots. The global tomography model of Priestley *et al.* (2018) indicates a thick lithosphere for the PaB, ranging from 150 to 180 km. The major discrepancy between our group velocity model and the SL2013sv one is in the central Andean region. The SL2013sv model exhibits a long-wavelength positive *S*-wave velocity perturbation starting at a depth of 100 km that becomes stronger at a depth of 150 km. This could be indicative of the imaging of the central Andean lithosphere bottom. Our maps, however, do not present any structure that correlates with this positive *S*-velocity anomaly feature. The Rayleigh group velocity estimates of Rosa *et al.* (2016b) and the *S*-velocity model of Feng *et al.* (2004) also do not support the existence of such structure at these depths, suggesting that vertical smearing may have caused the subducting Nazca lithosphere to be shallower on the SL2013sv maps. The model of Priestley *et al.* (2018) shows a lithosphere thickness ranging from 170 to 220 km, for the central Andean region, which could be the sum of a thickened Andean lithosphere due to flexural topographic load (e.g. Pérez-Gussinyé *et al.* 2008) with the subducting Nazca lithosphere.

Slow group velocities may be identified in the uppermost mantle underneath the BP, MP, PtB and also along the CTB and CB and are in agreement with the low *S*-velocity anomalies from the SL2013sv model. These slow group velocities and *S*-velocity anomalies are probably related to lithospheric thinning in these regions. Heit *et al.* (2007) estimate values of 80 km for the BP and MP lithospheres, while the model of Priestley *et al.* (2018) shows estimates of 90, 70 and 80 km for the PtB, CTB and CB lithospheres, respectively. Our group velocity maps, however, do show a more prominent slow velocity anomaly underneath the BP than that observed in the SL2013sv model.

Another interesting feature observed on the maps in Fig. 13 is the presence of a strong velocity gradient between the PB and CB, which roughly coincides with the location of the Western Paraná Suture (WPS) (Dragone *et al.* 2017), a continental-scale gravity discontinuity. From the analysis of a newly derived gravity map and crustal gravity modelling, integrated with other geophysical and geological information, Dragone *et al.* (2017) proposed the existence of a Neoproterozoic-Cambrian suture/shear zone separating the PB, to the east, from the PcB, RAC, CTB, RTC, CB, to the west and from RPC to the south. A composite shear wave model of Shirzad *et al.* (2019) shows a strong velocity contrast between the lower crust of the PB and CB, which are consistent with the proposed location of the WPS. A magnetotelluric transect experiment perpendicular to the WPS along the RPC and PB was used by Bologna *et al.* (2019) to derive a geoelectrical lithospheric model for this region. At depths of 50–60 km, a large electrical conductor was imaged exactly beneath the WPS, separating a more resistive and thick RPC lithosphere from a more conductive one underneath the PB. As indicated by our group velocity models, this suture may extend to lithospheric depths.

4.5 Inversion for 1-D *S*-velocity depth profiles

As Rayleigh waves are primarily sensitive to shear-velocity variations, we estimate 1-D *S*-velocity depth profiles at ten locations from our 2-D group velocity maps. As an initial model for the linearized inversion method of Herrmann & Ammon (2002), we use the 1-D velocity and density structure from the AK135 model. The model was parameterized with two crustal layers and an upper mantle half-space, for the first 200 km. The thickness of each layer and the Poisson ratio are fixed and we assume an isotropic structure. In Fig. 14, we present 1-D *S*-velocity models for the CTB, BP, AmC, PB, TP, AcB, APVC, MP, PaB and SFC, after a good adjustment of the dispersion curves was achieved, along with their respective regionalized dispersion (in green) and predicted dispersion (in blue) curves from the best *S*-velocity model estimated during the inversion process. In Fig. 14(a), the *S*-velocity profile for the CTB shows a slower shear wave velocity within the crust and the upper mantle compared to the *S*-velocity structure from the AK135, plotted in red. This result closely agrees with the *S*-velocity profile taken from the SL2013sv model.

The estimated *S*-velocity structure profile for the crust beneath BP (Fig. 14b) presents values close to the AK135 model, but an increase is observed at a depth of about 35 to 75 km when an abrupt decrease is then detected, going up to a depth of 150 km. The shear wave velocity estimated for this interval is lower than those from the AK135 and SL2013sv models. The discrepancy between our *S*-velocity profile and the SL2013sv is most likely due to the increased ray path coverage of our study, which could have been able to better resolve the velocity structure beneath this region. It is worth mentioning that the *S*-velocity depth profile from the SL2013sv is practically the same as that from the AK135 model, possibly indicating a poorer adjustment for the BP. This decreased *S*-velocity in our model may be due to a lithosphere thinning beneath the BP. Heit *et al.* (2007) determined that the LAB would be at a depth of 80 km beneath the RCBR station, close to the Depression Sertaneja. More recently, Priestley *et al.* (2018) in a global study show values less than 100 km for the lithosphere thickness under the BP. The *P*-wave seismic tomography model of Simões Neto *et al.* (2019) for the BP exhibits negative velocity anomalies within the lithosphere and in the sublithospheric mantle, which, if interpreted in terms of temperature, could indicate the presence of hotter material at shallower depths. Garcia *et al.* (2019) derived a 3-D geoelectrical model from a long-term magnetotelluric profile, almost north–south, in the western part of the BP, and found a strong electrical conductor beneath the Araripe Basin. This electrical conductor was interpreted as indicative of asthenospheric material at shallower depths, favouring the hypothesis of lithospheric thinning. Another evidence that would support this idea is the compiled heat flow measurements map of Hamza & Muñoz (1996). The values of heat flow in the region are high, with an average value of 80 mW m^{-2}, compatible with a lithosphere–asthenosphere limit at approximately 80 km in depth. The BP has been in the epeirogenesis

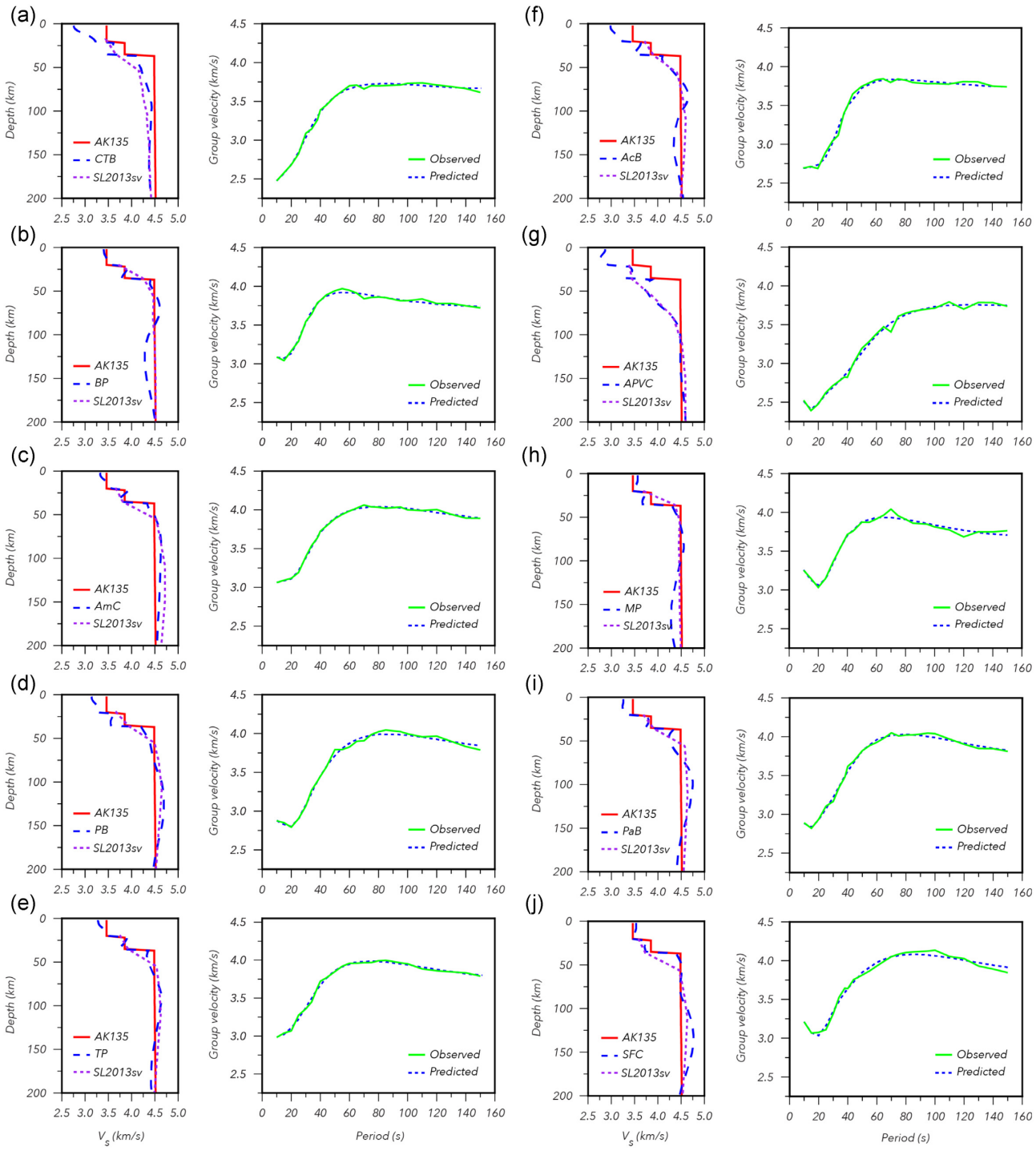

Figure 14. 1-D *S*-velocity depth profiles for ten different locations shown as black-white dots in Fig. 13 in the first and third columns, along with group velocity dispersion curves, in the second and fourth columns. The 1-D profiles and the dispersion curves are for the following regions: (a) CTB: Chaco-Tarija Basin, (b) BP: Borborema Province, (c) AmC: Amazonian Craton, (d) PB: Paraná Basin, (e) TP: Tocantins Province, (f) AcB: Acre Basin, (g) APVC: Altiplano-Puna volcanic complex, (h) MP: Mantiqueira Province, (i) PaB: Parnaíba Basin and (j) SFC: São Francisco Craton. In the first and third columns, the inverted 1-D *S*-velocity depth profiles are in blue, the *S*-velocity structure of the reference model AK135 is plotted in red, and the *S*-velocity profiles taken from the model SL2013sv are in purple. The second and fourth columns present regionalized dispersion (in green) and predicted dispersion (in blue) curves from the best *S*-velocity model estimated during the inversion process.

process since the Cretaceous, with the main topographic signatures being the Borborema Plateau, the Depression Sertaneja, the Chapada do Araripe and some other residual plateaus. Studies of apatite fission-track suggest the existence of two palaeothermal events in the BP: the first, a cooling event between 100 and 90 Ma and the second, in the Neogene, between 0 and 20 Ma (Morais Neto *et al.* 2009). According to Morais Neto *et al.* (2009), if these events are related to uplifts, they represent the main epeirogenic events in the

BP. Among the mechanisms postulated to explain the epeirogenesis and the Cenozoic structure of the BP, the following stand out: the passage of the BP over a deep mantle plume that would be located under the Fernando de Noronha archipelago (Jardim de Sá *et al.* 1999), thermal uplift caused by a thermal anomaly in the upper mantle (Ussami *et al.* 1999a; Chaves & Ussami 2010), lithospheric delamination (Silveira 2006; Lima *et al.* 2015), erosion of the lithosphere generated by an edge convection cell (Hollanda *et al.* 2006; Knesel *et al.* 2011), magmatic underplating (Magnavita *et al.* 1994; Oliveira & de Medeiros 2012) and, finally, adjacent lithospheric thickening and thermal rebalancing triggered by the lithospheric flow during the Mesozoic extension (Morais Neto *et al.* 2009). Using a numerical model that combines weathering, erosion, sedimentation, sea level changes, flexural isostasy and thermal effects due to the lithospheric stretch to simulate the tectonosedimentary evolution of the BP from the Lower Cretaceous, Sacek *et al.* (2019) show that approximately 70 per cent of the regional elevation observed in the BP post-rift can be explained by differential denunciation of the continent and flexural rebound of the lithosphere. The remaining elevation, according to Sacek *et al.* (2019), could be explained by a thermal component in the mantle induced by partial erosion of the continental lithosphere base under the BP due to the edge-driven convection mechanism (King & Anderson 1998). Such a mechanism, therefore, requires the lithosphere beneath the BP to be thinned.

In Fig. 14(c), the estimated *S*-velocity structure beneath AmC shows a faster lithospheric lid when compared to the AK135 *S*-velocity structure, as expected for a thick cratonic lithosphere, and in good agreement with the profile from SL2013sv model up to a depth of 100 km. Below this depth, our inverted 1-D *S*-velocity shows a decrease in shear wave velocity in relation to the SL2013sv model. A slow shear-velocity is estimated within the crust of the PB compared to the AK135 model, while a faster shear wave velocity is estimated for the PB lithosphere, going to at least a depth of 150 km, which indicates a thick lithosphere under this basin (Fig. 14d). Our 1-D *S*-velocity profile matches very well the *S*-velocity profile from the SL2013sv. A thick lithosphere along with high shear wave velocity are results used to argue in favour of a cratonic character to the PB lithosphere, but recently published studies have challenged this view (e.g. Padilha *et al.* 2015; Chaves *et al.* 2016; Bologna *et al.* 2019).

For the 1-D *S*-velocity structure under the TP, Fig. 14(e) exhibits an increase of shear wave velocity in relation to the AK135 model, from 50 km depth to about 90 km depth. Below this depth interval, the *S*-velocity starts to decrease and becomes slower than that from the AK135 model. This change from fast to slow shear wave velocity may be associated with the LAB. The *S*-velocity depth profile from the SL2013sv model presents the same tendency as our model.

In comparison to the AK135 model, the AcB profile in Fig. 14(f) presents slower *S*-velocity for the crust and upper mantle, which increases down to ∼75 km depth, agreeing with the profile from SL2013sv model. Then, suddenly, the shear-velocity decreases again from 90 to 140 km depth. The global thickness model of Priestley *et al.* (2018) estimates that the LAB in this region is at a depth of around 140 km. We think that the modelled decreased *S*-velocity at a depth of 75 km is due to the presence of a mid-lithosphere discontinuity (MLD), a portion of the lithosphere that presents significant drops (2–6 per cent) in seismic velocity (Karato *et al.* 2015). Nonetheless, further *S*-receiver function studies are required in this area to properly determine the nature of upper mantle discontinuities.

The slowest group velocities of the South American continent shown in Figs 11(c) and (d), related to the APVC, are also reflected on the profile of Fig. 14(g), with *S*-velocity values as low as ∼2.8 km s^{-1} for the shallow velocity structure, progressively increasing with depth until a convergence with the AK135 velocities is reached. Our 1-D *S*-velocity profile for the APVC presents a good match with the *S*-velocity profile from the SL2013sv model.

The 1-D *S*-velocity model under the MP (Fig. 14h) presents a crustal velocity structure similar to the AK135 one, followed by an increased velocity in the upper mantle down to about 90 km depth. Below this depth, the model reveals a decreased *S*-velocity value that is not observed in the SL2013sv model and it is most likely related to the LAB. A thinner lithosphere may be expected for the transition from continental to oceanic lithosphere such as the MP, due to the stretching caused by the Atlantic Ocean opening. However, it is worth mentioning that surface wave tomography has limited vertical resolution (e.g. Rychert & Shearer 2009) and therefore it is not possible to quantitatively determine a depth at which the LAB occurs, that is, we observe a smooth velocity decrease in this case from 90 to about 150 km depth, but our profile does not show any sharp velocity discontinuity. The SL2013sv profile does not exhibit a velocity inversion and is actually very close to the AK135 profile, which may indicate a poorer adjustment for the MP, similar to that of the BP.

For the PaB (Fig. 14i), our profile shows slower velocities for the upper crust than those from the AK135 model, while the discrepancy between both profiles for the lower crust is less prominent. Note that the sharp velocity discontinuities at 20 and 35 km depth are in fact inherited from the initial model and that the PaB crust is more likely thicker, with the Moho discontinuity at a depth of about 40 km (Daly *et al.* 2014). An increase of *S*-velocity from about 45 to 100 km depth is observed in our profile, but it is not consistent with the *S*-velocity profile taken from the SL2013sv model. Priestley *et al.* (2018) estimate lithospheric thicknesses from 150 to 180 km for the PaB, which seems to be overall correlated with a strong velocity drop from 100 to 180 km revealed by our model. In this case, the SL2013sv model also presents a decrease in velocity for lithospheric depths, but it is less pronounced than the one shown by our model. The fact that the velocity starts to invert at 100 km may be due to the presence of a MLD, but more evidence is required to support the presence of this discontinuity beneath the PaB.

Finally, in Fig. 14(j), the shallow velocity structure for the SFC down to ∼85 km depth is very similar between our *S*-velocity profile and the AK135 model, while a decreased velocity is noted in the SL2013sv model. Below the depth of 85 km, an increased velocity is perceived both in our model and the SL2013sv model, in comparison to the AK135. From 140 km depth onwards, the velocity in our model starts to decrease, coherent with a deep LAB beneath a thick and stable cratonic area. This behaviour is also notable in the SL2013sv profile.

5 CONCLUSIONS

Deployment of new seismic stations by the RSBR (Rede Sismográfica Brasileira) and other temporary networks such as XC (Pantanal, Chaco and Paraná structural studies) has greatly improved the coverage in the South American Platform, allowing higher resolution tomography models to be constructed. From 282 receivers and 1043 earthquakes, we obtain 17 838 Rayleigh wave dispersion curves distributed over South America, which are used to

produce 2-D regionalized group velocity maps in the period range of 10–150 s. Inversion of group velocity data using a combination of FMM, to solve the forward problem with a subspace method to solve the inverse step, provides a stable and robust way to estimate regional group velocity variation maps, in which the non-linearity of the problem is taken into account iteratively.

Long-wavelength features of South America detected by previous surface wave tomography studies are also present in our model, as the AmC and SFC, imaged as fast group velocities, the PB, CB, AmB, CTB, Madre de Dios, Llanos, Oriente-Marañón, Ucayali basins, imaged as slow group velocities on short period maps, and a notable elongated anomaly along the western border of the South American continent following the Andes, imaged as a strong slow group velocity, particularly at intermediate periods.

Due to our more dense and homogeneous source–receiver path distribution, small-scale structures that were absent or not well constrained in previous models, as the Tucano-Jatobá, Pantanal and Llanos basins, and the São Luís, Rio Apa and Rio Tebicuary cratons, could be illuminated, especially at periods of 10 and 20 s. Comparison of our short period maps with the CRUST1.0 and UNB_TopoDens models indicates an excellent correlation between sedimentary basins, including thin ones, such as Parecis Basin, and slow group velocity, as well as areas of exposed basement and fast group velocity. Fast group velocity heterogeneities in the AmC, at the period of 20 s, correlate well with the location of the following geochronological provinces (Tassinari & Macambira 1999): Central-Amazonian, Maroni-Itacaiúnas, Ventuari-Tapajós, Rio Negro-Juruena and Sunsás.

At the intermediate periods of 40 and 50 s, group velocities are sensitive to crustal velocity and thickness. Regions with thick crust as the central Andes, for example, tend to present decreased group velocity because slower crustal rocks are being sampled at deeper depths while areas with thin crust tend to present fast velocity due to mantle rocks placed at shallower depths. Fast group velocities are observed beneath the BP and MP, where crustal thickness varies from thin to normal. In the PB and CB, slow group velocities at the period of 40 s are consistent with those of the ambient tomography of Shirzad *et al.* (2019), and may be caused by the sedimentary package load, which bends the crust to greater depths. A highly variable crustal thickness in the AmC, detected by the receiver function study of Albuquerque *et al.* (2017), is reflected on our intermediate period maps as an alternating pattern of fast and slow group velocities, chiefly along the AmB and SmB. The most striking feature of our map of 40 s is a fast group velocity structure with the same NE trend of the Transbrasiliano lineament (TBL) that correlates with a zone of low analytic signal of the magnetic field from the model of Fairhead & Maus (2003) and is also present on the magnetic anomaly map EMAG2v3 of Meyer *et al.* (2017), as a positive amplitude magnetic anomaly.

The lithospheric structure retrieved by the long period maps of 100 and 150 s presents a good agreement with the SL2013sv model of Schaeffer & Lebedev (2013), except in the central Andean region, where the SL2013sv slices at 100 and 150 km depth show a fast *S*-velocity anomaly that is not present on our maps, nor in previous models of Rosa *et al.* (2016b) and Feng *et al.* (2004). A strong velocity discontinuity between the PB and CB on our maps of 100 and 150 s might indicate that the Western Paraná Suture Dragone *et al.* (2017) extends further to lithospheric depths.

As a step towards generating a 3-D shear velocity model for the upper mantle beneath South America, which we intend to provide in another study, we present 1-D *S*-velocity depth profiles at ten locations: CTB, BP, AmC, PB, TP, AcB, APVC, MP, PaB and SFC. In general, our inverted profiles are consistent with the SL2013sv model. Nonetheless, for the BP, AcB and MP profiles, our estimates are in disagreement with predictions from the SL2013sv model. Beneath the BP, for example, a decrease in shear-wave velocity, compared to the *S*-velocity structure from the AK135 model, at a depth from about 75 to 150 km, is a feature that is not present in the SL2013sv model, and it was possibly detected because of our denser ray path coverage. This decreased *S*-velocity is in agreement with the hypothesis of lithospheric thinning beneath the BP, which is also supported by *S* receiver function estimates for the depth of the LAB (Heit *et al.* 2007), negative *P*-wave velocity anomalies (Simões Neto *et al.* 2019) and high heat flow with an average of 80 mW m^{-2} (Hamza & Muñoz 1996). According to Sacek *et al.* (2019), approximately 30 per cent of the elevation of the BP post-rift can be explained by a thermal component in the mantle that requires the lithosphere to be thinned. Although the AcB profile shows slower *S*-velocity for the crust and upper mantle down to ∼60 km depth, as we observe for the profile from the SL2013sv model, below this depth the profiles no longer match. From 60 to 75 km depth, the *S*-velocity increases and it is faster than the AK135 model, while the *S*-velocity from the SL2013sv model remains very close to the *S*-velocity structure from the AK135 model. From 75 to 140 km depth, the *S*-velocity from our model decreases, leading us to suggest the presence of a mid-lithosphere discontinuity beneath the AcB. The *S*-velocity profile under the MP presents a crustal and uppermost mantle velocity structure similar to the AK135 model. However, down to about 90 km depth, the *S*-velocity decreases and remains lower than the values provided by the AK135 model. For this same depth interval, the SL2013sv profile is very close to the AK135 profile. The *S*-velocity inversion at the depth of 90 km in our profile may be related to the LAB because a thinner lithosphere is expected for the MP due to the stretching caused by the Atlantic Ocean opening.

ACKNOWLEDGEMENTS

We thank Marcelo Assumpção for providing us access to data from the XC seismic network (FAPESP Thematic Project - 2013/24215-6). CAPES (Coordenação de Aperfeiçoamento de Pessoal de Nível Superior) sponsored a Master scholarship to AVSN, CNPq (Conselho Nacional de Desenvolvimento Científico e Tecnológico) granted a Research Fellowship (PQ-1D, 307251/2016-0) to GSF. This research was also supported by CNPq through the INCT-ET (Instituto Nacional de Ciências e Tecnologia em Estudos Tectônicos) (Grant number 465613/2014-4). All figures were produced using the GMT software (Wessel *et al.* 2013). We thank editor Andrea Morelli and two anonymous reviewers for their helpful comments that improved the original version of this manuscript.

DATA AVAILABILITY STATEMENT

Seismic data were fetched through HTTP GET requests to the USP Seismological Center (http://seisrequest.iag.usp.br/fdsnws/dataselect/1/) and to the IRIS Data Management Center (http://service.iris.edu/fdsnws/dataselect/1/). Additional data from the OS and XC seismic networks are restricted. We use the Computer Programs in Seismology (CPS) package of Herrmann (2013) available at http://www.eas.slu.edu/eqc/eqccps.html/. We use the Fast Marching Surface Tomography (FMST) package of Rawlinson (2005) available at http://rses.anu.edu.au/~nick/surftomo.html.

REFERENCES

Affonso, G.M.P.C. *et al.*, 2021. Lithospheric architecture of the Paranapanema Block and adjacent nuclei using multiple-frequency P-wave seismic tomography, *J. geophys. Res.,* **126,** e2020JB021183, doi:10.1029/2020JB021183.

Albuquerque, D.F., França, G.S., Moreira, L.P., Assumpção, M., Bianchi, M., Barros, L.V., Quispe, C.C. & Oliveira, M.E., 2017. Crustal structure of the Amazonian Craton and adjacent provinces in Brazil, *J. South Am. Earth Sci.,* **79,** 431–442.

Almeida, F.F.M.D., Hasui, Y., Brito Neves, B.B.D. & Fuck, R.A., 1981. Brazilian structural provinces: an introduction, *Earth-Sci. Rev.,* **17**(1–2), 1–29.

Almeida, F.F.M.D., Brito Neves, B.B.D. & Carneiro, C.D.R., 2000. The origin and evolution of the South American Platform, *Earth-Sci. Rev.,* **50**(1–2), 77–111.

Amante, C. & Eakins, B., 2009. ETOPO1 1 arc-minute global relief model: procedures, data sources and analysis, NOAA Technical Memorandum NESDIS NGDC-24, National Geophysical Data Center, Marine Geology and Geophysics Division, Boulder, CO, USA.

Assine, M.L., Merino, E.R., Pupim, F.N., Warren, L.V., Guerreiro, R.L. & McGlue, M.M., 2015. Geology and geomorphology of the Pantanal Basin, in *Dynamics of the Pantanal Wetland in South America,* pp. 23–50, Springer.

Aster, R.C., Borchers, B. & Thurber, C.H., 2018. *Parameter Estimation and Inverse Problems,* Elsevier.

Azevedo, P.A., Rocha, M.P., Soares, J.E.P. & Fuck, R.A., 2015. Thin lithosphere between the Amazonian and São Francisco cratons, in central Brazil, revealed by seismic P-wave tomography, *Geophys. J. Int.,* **201**(1), 61–69.

Baby, P., Rivadeneira, M., Barragán, R. & Christophoul, F., 2013. Thick-skinned tectonics in the Oriente foreland basin of Ecuador, *Geol. Soc., Lond., Spec. Publ.,* **377**(1), 59–76.

Barros, L.V. & Assumpção, M., 2011. Basement depths in the Parecis Basin (Amazon) with receiver functions from small local earthquakes in the Porto dos Gaúchos seismic zone, *J. South Am. Earth Sci.,* **32**(2), 142–151.

Bianchi, M.B. *et al.*, 2018. The Brazilian Seismographic Network (RSBR): improving seismic monitoring in Brazil, *Seismol. Res. Lett.,* **89**(2A), 452–457.

Bishop, B.T., Beck, S.L., Zandt, G., Wagner, L.S., Long, M.D. & Tavera, H., 2018. Foreland uplift during flat subduction: insights from the Peruvian Andes and Fitzcarrald Arch, *Tectonophysics,* **731,** 73–84.

Bologna, M.S., Dragone, G.N., Muzio, R., Peel, E., Nuñez-Demarco, P. & Ussami, N., 2019. Electrical structure of the lithosphere from Rio de la Plata Craton to Paraná Basin: amalgamation of cratonic and refertilized lithospheres in SW Gondwanaland, *Tectonics,* **38**(1), 77–94.

Brito Neves, B.B.D. & Fuck, R.A., 2013. Neoproterozoic evolution of the basement of the South-American platform, *J. South Am. Earth Sc.,* **47,** 72–89.

Brito Neves, B.B.D. & Fuck, R.A., 2014. The basement of the South American platform: half Laurentian (N-NW)+ half Gondwanan (E-SE) domains, *Precambrian Res.,* **244,** 75–86.

Brito Neves, B.B.D., Fuck, R.A. & Pimentel, M.M., 2014. The Brasiliano collage in South America: a review, *Braz. J. Geol.,* **44**(3), 493–518.

Brod, J.A., Barbosa, E.S.R., Junqueira-Brod, T.C., Gaspar, J.C., Diniz-Pinto, H.S., Sgarbi, P.B.A. & Petrinovic, I.A., 2005. The Late-Cretaceous Goiás Alkaline Province (GAP), Central Brazil, in *Mesozoic to Cenozoic Alkaline Magmatism in the Brazilian Plataform. Edusp/Fapesp,* pp. 261–316.

Chaves, C., Ussami, N. & Ritsema, J., 2016. Density and P-wave velocity structure beneath the Paraná Magmatic Province: refertilization of an ancient lithospheric mantle, *Geochem. Geophys. Geosyst.,* **17**(8), 3054–3074.

Chaves, C. A.M. & Ussami, N., 2010. Upper mantle density anomaly under the Borborema Province (NE Brazil) derived from inversion of geoid anomalies: new constraint on its continental margin evolution, *EOS, Trans. Am. Geophys. Un.,* **91**(26), abstract S23B-05.

Cordani, U.G., Cubas, N., Nutman, A.P., Sato, K., Gonzales, M.E. & Presser, J.L.B., 2001. Geochronological constraints for the evolution of the metamorphic complexes near the Tebicuary river, southern Precambrian region of Paraguay, in *Proceedings of the 3rd South American Symposium on Isotope Geology,* Servicio Nacional de Geologia y Mineria, Chile.

Cordani, U.G., Teixeira, W., D'Agrella-Filho, M. & Trindade, R., 2009. The position of the Amazonian Craton in supercontinents, *Gondwana Res.,* **15**(3–4), 396–407.

Cordani, U.G., Teixeira, W., Tassinari, C.C.G., Coutinho, J.M.V. & Ruiz, A.S., 2010. The Rio Apa Craton in Mato Grosso do Sul (Brazil) and northern Paraguay: geochronological evolution, correlations and tectonic implications for Rodinia and Gondwana, *Am. J. Sci.,* **310**(9), 981–1023.

Cordani, U.G., Pimentel, M.M., de Araújo, C.E.G. & Fuck, R.A., 2013. The significance of the Transbrasiliano-Kandi tectonic corridor for the amalgamation of West Gondwana, *Braz. J. Geol.,* **43**(3), 583–597.

Costa, I.S.L., Rocha, M.P., Klein, E.L. & Vasquez, M.L., 2020. Lithospheric structure of the southern Amazonian Craton from multiple-frequency seismic tomography: preliminary insights on tectonic and metallogenic implications, *J. South Am. Earth Sci.,* **101,** doi:10.1016/j.jsames.2020.102608.

Costa, J., Hasui, Y., Bemerguy, R.L., Soares-Júnior, A.V. & Villegas, J., 2002. Tectonics and paleogeography of the Marajó Basin, northern Brazil, *Anais da Academia Brasileira de Ciências,* **74**(3), 519–531.

Daly, M.C., Andrade, V., Barousse, C.A., Costa, R., McDowell, K., Piggott, N. & Poole, A.J., 2014. Brasiliano crustal structure and the tectonic setting of the Parnaíba basin of NE Brazil: results of a deep seismic reflection profile, *Tectonics,* **33**(11), 2102–2120.

De Silva, S.L., 1989. Altiplano-Puna volcanic complex of the central Andes, *Geology,* **17**(12), 1102–1106.

Dragone, G.N., Ussami, N., Gimenez, M.E., Klinger, F.G.L. & Chaves, C.A.M., 2017. Western Paraná suture/shear zone and the limits of Rio Apa, Rio Tebicuary and Rio de la Plata cratons from gravity data, *Precambrian Res.,* **291,** 162–177.

Dutra, A.C., Marangoni, Y.R. & Junqueira-Brod, T.C., 2012. Investigation of the Goiás Alkaline Province, Central Brazil: application of gravity and magnetic methods, *J. South Am. Earth Sci.,* **33**(1), 43–55.

Dziewonski, A., Bloch, S. & Landisman, M., 1969. A technique for the analysis of transient seismic signals, *Bull. seism. Soc. Am.,* **59**(1), 427–444.

Espurt, N. *et al.*, 2007. How does the Nazca Ridge subduction influence the modern Amazonian foreland basin?, *Geology,* **35**(6), 515–518.

Fairhead, J.D. & Maus, S., 2003. CHAMP satellite and terrestrial magnetic data help define the tectonic model for South America and resolve the lingering problem of the pre-break-up fit of the South Atlantic Ocean, *Leading Edge,* **22**(8), 779–783.

Fang, H., Zhang, H., Yao, H., Allam, A., Zigone, D., Ben-Zion, Y., Thurber, C. & van der Hilst, R.D., 2016. A new algorithm for three-dimensional joint inversion of body wave and surface wave data and its application to the Southern California plate boundary region, *J. geophys. Res.,* **121**(5), 3557–3569.

Feng, M., Assumpçao, M. & Van der Lee, S., 2004. Group-velocity tomography and lithospheric S-velocity structure of the South American continent, *Phys. Earth planet. Inter.,* **147**(4), 315–331.

Feng, M., Van der Lee, S. & Assumpção, M., 2007. Upper mantle structure of South America from joint inversion of waveforms and fundamental mode group velocities of Rayleigh waves, *J. geophys. Res.,* **112**(B4), doi:10.1029/2006JB004449.

Fianco, C.B., França, G.S., Albuquerque, D.F., Vilar, C.D.S. & Argollo, R.M., 2019. Using the receiver function for studying earth deep structure in the Southern Borborema Province, *J. South Am. Earth Sci.,* **94,** doi:10.1016/j.jsames.2019.102221.

França, G.S. & Assumpção, M., 2004. Crustal structure of the Ribeira fold belt, SE Brazil, derived from receiver functions, *J. South Am. Earth Sci.,* **16**(8), 743–758.

Garcia, X., Julià, J., Nemocón, A.M. & Neukirch, M., 2019. Lithospheric thinning under the Araripe Basin (NE Brazil) from a long-period magnetotelluric survey: constraints for tectonic inversion, *Gondwana Res.,* **68,** 174–184.

Gomes, C.B. & Comin-Chiaramonti, P., 2005. Some notes on the Alto Paranaíba igneous province, in *Mesozoic to Cenozoic Alkaline Magmatism in the Brazilian Platform,* pp. 317–340, FAPESP.

Gurnis, M., Mitrovica, J.X., Ritsema, J. & van Heijst, H.-J., 2000. Constraining mantle density structure using geological evidence of surface uplift rates: the case of the African superplume, *Geochem. Geophys. Geosyst.,* **1**(7), doi:10.1029/1999GC000035.

Hamza, V.M. & Muñoz, M., 1996. Heat flow map of South America, *Geothermics,* **25**(6), 599–646.

Heintz, M., Debayle, E. & Vauchez, A., 2005. Upper mantle structure of the South American continent and neighboring oceans from surface wave tomography, *Tectonophysics,* **406**(1–2), 115–139.

Heit, B., Sodoudi, F., Yuan, X., Bianchi, M. & Kind, R., 2007. An S receiver function analysis of the lithospheric structure in South America, *Geophys. Res. Lett.,* **34**(14), doi:10.1029/2007GL030317.

Herrin, E. & Goforth, T., 1977. Phase-matched filters: application to the study of Rayleigh waves, *Bull. seism. Soc. Am.,* **67**(5), 1259–1275.

Herrmann, R.B., 2013. Computer programs in seismology: an evolving tool for instruction and research, *Seismol. Res. Lett.,* **84**(6), 1081–1088.

Herrmann, R.B. & Ammon, C.J., 2002. *Computer Programs in Seismology: Surface Waves, Receiver Functions and Crustal Structure,* Saint Louis University.

Hollanda, M.H.B.M., Pimentel, M.M., Oliveira, D.C. & Jardim de Sá, E.F., 2006. Lithosphere–asthenosphere interaction and the origin of Cretaceous tholeiitic magmatism in Northeastern Brazil: Sr–Nd–Pb isotopic evidence, *Lithos,* **86**(1–2), 34–49.

Jardim de Sá, E.F., Matos, R.M.D., Moarais Neto, J.M., Saadi, A. & Pessoa Neto, O.C., 1999. Epirogenia cenozóica na Província Borborema: síntese e discussão sobre os modelos de deformação associados, in *Proceedings of the 7th Simpósio Nacional de Estudos Tectônicos, Lençóis,* pp. 58–61.

Julià, J., Assumpção, M. & Rocha, M.P., 2008. Deep crustal structure of the Paraná Basin from receiver functions and Rayleigh-wave dispersion: evidence for a fragmented cratonic root, *J. geophys. Res.,* **113**(B8), doi:10.1029/2007JB005374.

Karato, S.-I., Olugboji, T. & Park, J., 2015. Mechanisms and geologic significance of the mid-lithosphere discontinuity in the continents, *Nat. Geosci.,* **8**(7), 509–514.

Kennett, B.L.N., Sambridge, M.S. & Williamson, P.R., 1988. Subspace methods for large inverse problems with multiple parameter classes, *Geophys. J. Int.,* **94**(2), 237–247.

Kennett, B.L.N., Engdahl, E.R. & Buland, R., 1995. Constraints on seismic velocities in the Earth from traveltimes, *Geophys. J. Int.,* **122**(1), 108–124.

King, S.D. & Anderson, D.L., 1998. Edge-driven convection, *Earth planet. Sci. Lett.,* **160**(3–4), 289–296.

Klein, E.L., Moura, C.A.V. & Pinheiro, B.L.S., 2005. Paleoproterozoic crustal evolution of the São Luís Craton, Brazil: evidence from zircon geochronology and Sm-Nd isotopes, *Gondwana Res.,* **8**(2), 177–186.

Knesel, K.M., Souza, Z.S., Vasconcelos, P.M., Cohen, B.E. & Silveira, F.V., 2011. Young volcanism in the Borborema Province, NE Brazil, shows no evidence for a trace of the Fernando de Noronha plume on the continent, *Earth planet. Sci. Lett.,* **302**(1–2), 38–50.

Laske, G., Masters, G., Ma, Z. & Pasyanos, M., 2013. Update on CRUST1.0—a 1-degree global model of Earth's crust, in *Proceedngs of the EGU General Assembly 2013,* held 7–12 April 2013, Vienna, Austria, id. EGU2013-2658.

Lévêque, J.-J., Rivera, L. & Wittlinger, G., 1993. On the use of the checkerboard test to assess the resolution of tomographic inversions, *Geophys. J. Int.,* **115**(1), 313–318.

Lima, M.V.A.G.d., Berrocal, J., Soares, J.E.P. & Fuck, R.A., 2015. Deep seismic refraction experiment in northeast Brazil: new constraints for Borborema province evolution, *J. South Am. Earth Sci.,* **58,** 335–349.

Luz, R.M.N., Julià, J. & do Nascimento, A.F., 2015. Crustal structure of the eastern Borborema Province, NE Brazil, from the joint inversion of receiver functions and surface wave dispersion: implications for plateau uplift, *J. geophys. Res.,* **120**(5), 3848–3869.

Magnavita, L.P., Davison, I. & Kusznir, N.J., 1994. Rifting, erosion, and uplift history of the Recôncavo-Tucano-Jatobá Rift, northeast Brazil, *Tectonics,* **13**(2), 367–388.

Mantovani, M.S.M., Louro, V.H.A., Ribeiro, V.B., Requejo, H.S. & dos Santos, R.P.Z., 2016. Geophysical analysis of Catalão I alkaline–carbonatite complex in Goiás, Brazil, *Geophys. Prospect.,* **64**(1), 216–227.

Meyer, B., Saltus, R. & Chulliat, A., 2017. EMAG2: Earth magnetic anomaly grid (2-arc-minute resolution), version 3, National Centers for Environmental Information, NOAA.

Mora, A. *et al.*, 2019. Tectonic evolution of petroleum systems within the onshore Llanos Basin: insights on the presence of Orinoco heavy oil analogs in Colombia and a comparison with other heavy oil provinces worldwide, *AAPG Bull.,* **103**(5), 1179–1224.

Morais Neto, J.M., Hegarty, K.A., Karner, G.D. & Alkmim, F.F.D., 2009. Timing and mechanisms for the generation and modification of the anomalous topography of the Borborema Province, northeastern Brazil, *Mar. Petrol. Geol.,* **26**(7), 1070–1086.

Oliveira, R.G.D. & de Medeiros, W.E., 2012. Evidences of buried loads in the base of the crust of Borborema Plateau (NE Brazil) from Bouguer admittance estimates, *J. South Am. Earth Sci.,* **37,** 60–76.

Oyhantçabal, P., Siegesmund, S. & Wemmer, K., 2011. The Río de la Plata Craton: a review of units, boundaries, ages and isotopic signature, *Int. J. Earth Sci.,* **100**(2), 201–220.

Padilha, A.L., Vitorello, Í., Antunes, C.E. & Pádua, M.B., 2015. Imaging three-dimensional crustal conductivity structures reflecting continental flood basalt effects hidden beneath thick intracratonic sedimentary basin, *J. geophys. Res.,* **120**(7), 4702–4719.

Pavão, C.G., França, G.S., Bianchi, M., de Almeida, T. & Von Huelsen, M.G., 2013. Upper-lower crust thickness of the Borborema Province, NE Brazil, using receiver function, *J. South Am. Earth Sci.,* **42,** 242–249.

Pérez-Gussinyé, M., Lowry, A., Phipps Morgan, J. & Tassara, A., 2008. Effective elastic thickness variations along the Andean margin and their relationship to subduction geometry, *Geochem. Geophys. Geosyst.,* **9**(2), doi:10.1029/2007GC001786.

Priestley, K., McKenzie, D. & Ho, T., 2018. A lithosphere–asthenosphere boundary—a global model derived from multimode surface-wave tomography and petrology, in *Lithospheric Discontinuities, Geophysical Monograph Series,* pp. 111–123, eds Yuan, H. & Romanowicz, B., AGU.

Rapela, C.W., Pankhurst, R.J., Casquet, C., Fanning, C.M., Baldo, E.G., González-Casado, J.M., Galindo, C. & Dahlquist, J., 2007. The Río de la Plata craton and the assembly of SW Gondwana, *Earth-Sci. Rev.,* **83**(1–2), 49–82.

Rawlinson, N., 2005. FMST: fast marching surface tomography package – instructions, Research School of Earth Sciences, Australian National University, Canberra, Australia.

Rawlinson, N. & Sambridge, M., 2004a. Multiple reflection and transmission phases in complex layered media using a multistage fast marching method, *Geophysics,* **69**(5), 1338–1350.

Rawlinson, N. & Sambridge, M., 2004b. Wave front evolution in strongly heterogeneous layered media using the fast marching method, *Geophys. J. Int.,* **156**(3), 631–647.

Rawlinson, N. & Sambridge, M., 2005. The fast marching method: an effective tool for tomographic imaging and tracking multiple phases in complex layered media, *Explor. Geophys.,* **36**(4), 341–350.

Rawlinson, N. & Spakman, W., 2016. On the use of sensitivity tests in seismic tomography, *Geophys. J. Int.,* **205**(2), 1221–1243.

Rawlinson, N., Reading, A.M. & Kennett, B.L., 2006. Lithospheric structure of Tasmania from a novel form of teleseismic tomography, *J. geophys. Res.,* **111**(B2), doi:10.1029/2005JB003803.

Rawlinson, N., Kennett, B.L.N., Vanacore, E., Glen, R.A. & Fishwick, S., 2011. The structure of the upper mantle beneath the Delamerian and Lachlan orogens from simultaneous inversion of multiple teleseismic datasets, *Gondwana Res.,* **19**(3), 788–799.

Rivadeneyra-Vera, C. *et al.*, 2019. An updated crustal thickness map of central South America based on receiver function measurements in the region of the Chaco, Pantanal, and Paraná Basins, southwestern Brazil, *J. geophys. Res.,* **124**(8), 8491–8505.

Rocha, M.P., Schimmel, M. & Assumpção, M., 2011. Upper-mantle seismic structure beneath SE and Central Brazil from P-and S-wave regional traveltime tomography, *Geophys. J. Int.,* **184**(1), 268–286.

Rocha, M.P., Assumpção, M., Affonso, G. M.P.C., Azevedo, P.A. & Bianchi, M., 2019a. Teleseismic P wave tomography beneath the Pantanal, Paraná, and Chaco-Paraná Basins, SE South America: delimiting lithospheric blocks of the SW Gondwana assemblage, *J. geophys. Res.,* **124**(7), 7120–7137.

Rocha, M.P., Azevedo, P.A., Assumpção, M., Pedrosa-Soares, A.C., Fuck, R. & Von Huelsen, M.G., 2019b. Delimiting the Neoproterozoic São Francisco Paleocontinental Block with P-wave traveltime tomography, *Geophys. J. Int.,* **219**(1), 633–644.

Roddaz, M., Viers, J., Brusset, S., Baby, P. & Hérail, G., 2005. Sediment provenances and drainage evolution of the Neogene Amazonian foreland basin, *Earth planet. Sci. Lett.,* **239**(1–2), 57–78.

Rosa, E.L.M.D., Vesely, F.F. & França, A.B., 2016a. A review on late Paleozoic ice-related erosional landforms in the Paraná Basin: origin and paleogeographical implications, *Braz. J. Geol.,* **46**(2), 147–166.

Rosa, M.L., Collaço, B., Assumpção, M., Sabbione, N. & Sánchez, G., 2016b. Thin crust beneath the Chaco-Paraná Basin by surface-wave tomography, *J. South Am. Earth Sci.,* **66,** 1–14.

Rychert, C.A. & Shearer, P.M., 2009. A global view of the lithosphere-asthenosphere boundary, *Science,* **324**(5926), 495–498.

Sacek, V., de Morais Neto, J.M., Vasconcelos, P.M. & de Oliveira Carmo, I., 2019. Numerical modeling of weathering, erosion, sedimentation, and uplift in a triple junction divergent margin, *Geochem. Geophys. Geosyst.,* **20**(5), 2334–2354.

Sambridge, M.S., 1990. Non-linear arrival time inversion: constraining velocity anomalies by seeking smooth models in 3-D, *Geophys. J. Int.,* **102**(3), 653–677.

Santos, T.J.S.D., Fetter, A.H. & Neto, J.A.N., 2008. Comparisons between the northwestern Borborema Province, NE Brazil, and the southwestern Pharusian Dahomey Belt, SW Central Africa, *Geol. Soc., Lond., Spec. Publ.,* **294**(1), 101–120.

Schaeffer, A.J. & Lebedev, S., 2013. Global shear speed structure of the upper mantle and transition zone, *Geophys. J. Int.,* **194**(1), 417–449.

Schimmel, M., Assumpçao, M. & VanDecar, J.C., 2003. Seismic velocity anomalies beneath SE Brazil from P and S wave traveltime inversions, *J. geophys. Res.,* **108**(B4), doi:10.1029/2001JB000187.

Sethian, J.A., 1996. A fast marching level set method for monotonically advancing fronts, *Proc. Natl. Acad. Sci.,* **93**(4), 1591–1595.

Sethian, J.A. & Popovici, A.M., 1999. 3-D traveltime computation using the fast marching method, *Geophysics,* **64**(2), 516–523.

Shapiro, N.M. & Singh, S.K., 1999. A systematic error in estimating surface-wave group-velocity dispersion curves and a procedure for its correction, *Bull. seism. Soc. Am.,* **89**(4), 1138–1142.

Sheng, M.B., Shaw, C., Vaníček, P., Kingdon, R.W., Santos, M. & Foroughi, I., 2019. Formulation and validation of a global laterally varying topographical density model, *Tectonophysics,* **762,** 45–60.

Shirzad, T., Assumpção, M. & Bianchi, M., 2019. Ambient seismic noise tomography in west-central and Southern Brazil, characterizing the crustal structure of the Chaco-Paraná, Pantanal and Paraná basins, *Geophys. J. Int.,* **220**(3), 2074–2085.

Silva, L.C., McNaughton, N.J., Armstrong, R., Hartmann, L.A. & Fletcher, I.R., 2005. The Neoproterozoic Mantiqueira Province and its African connections: a zircon-based U–Pb geochronologic subdivision for the Brasiliano/Pan-African systems of orogens, *Precambrian Res.,* **136**(3-4), 203–240.

Silveira, F.V., 2006. Magmatismo cenozóico da porção central do Rio Grande do Norte, NE do Brasil, *PhD thesis*, Universidade Federal do Rio Grande do Norte.

Silveira, G., Stutzmann, E., Griot, D.-A., Montagner, J.-P. & Victor, L.M., 1998. Anisotropic tomography of the Atlantic Ocean from Rayleigh surface waves, *Phys. Earth planet. Inter.,* **106**(3–4), 257–273.

Simões Neto, F.L., Julià, J. & Schimmel, M., 2019. Upper-mantle structure of the Borborema Province, NE Brazil, from P-wave tomography: implications for rheology and volcanism, *Geophys. J. Int.,* **216**(1), 231–250.

Tassinari, C.C.G. & Macambira, M.J.B., 1999. Geochronological provinces of the Amazonian Craton, *Episodes,* **22**(3), 174–182.

Teixeira, W., Cordani, U.G., Faleiros, F.M., Sato, K., Maurer, V.C., Ruiz, A.S. & Azevedo, E.J.P., 2020. The Rio Apa Terrane reviewed: UPb zircon geochronology and provenance studies provide paleotectonic links with a growing Proterozoic Amazonia, *Earth-Sci. Rev.,* **202,** doi:10.1016/j.earscirev.2020.103089.

Toczeck, A., Schmitt, R.S., Braga, M.A.S. & Miranda, F.P., 2019. Tectonic evolution of the Paleozoic Alto Tapajós intracratonic basin—a case study of a fossil rift in the Amazon Craton, *J. South Am. Earth Sci.,* **94,** doi:10.1016/j.jsames.2019.102225.

Torsvik, T.H., Smethurst, M.A., Burke, K. & Steinberger, B., 2006. Large igneous provinces generated from the margins of the large low-velocity provinces in the deep mantle, *Geophys. J. Int.,* **167**(3), 1447–1460.

Uba, C.E., Heubeck, C. & Hulka, C., 2006. Evolution of the late Cenozoic Chaco foreland basin, southern Bolivia, *Basin Res.,* **18**(2), 145–170.

Ussami, N., Karner, G.D. & Bott, M.H.P., 1986. Crustal detachment during South Atlantic rifting and formation of Tucano—Gabon basin system, *Nature,* **322**(6080), 629–632.

Ussami, N., Molina, E. & Medeiros, W., 1999a. Novos vínculos sobre a evolução térmica da margem continental leste do Brasil, *Simpósio Nacional de Estudos Tectônicos,* **7**(1999), 20–23.

Ussami, N., Shiraiwa, S. & Dominguez, J.M.L., 1999b. Basement reactivation in a sub-Andean foreland flexural bulge: the Pantanal wetland, SW Brazil, *Tectonics,* **18**(1), 25–39.

Van der Lee, S., James, D. & Silver, P., 2001. Upper mantle S velocity structure of central and western South America, *J. geophys. Res.,* **106**(B12), 30 821–30 834.

Van der Meer, D.G., Van Hinsbergen, D.J.J. & Spakman, W., 2018. Atlas of the underworld: slab remnants in the mantle, their sinking history, and a new outlook on lower mantle viscosity, *Tectonophysics,* **723,** 309–448.

VanDecar, J.C., James, D.E. & Assumpção, M., 1995. Seismic evidence for a fossil mantle plume beneath South America and implications for plate driving forces, *Nature,* **378**(6552), 25–31.

Vdovin, O., Rial, J.A., Levshin, A.L. & Ritzwoller, M.H., 1999. Group-velocity tomography of South America and the surrounding oceans, *Geophys. J. Int.,* **136**(2), 324–340.

Ward, K.M., Zandt, G., Beck, S.L., Christensen, D.H. & McFarlin, H., 2014. Seismic imaging of the magmatic underpinnings beneath the Altiplano-Puna volcanic complex from the joint inversion of surface wave dispersion and receiver functions, *Earth planet. Sci. Lett.,* **404,** 43–53.

Wessel, P., Smith, W.H., Scharroo, R., Luis, J. & Wobbe, F., 2013. Generic mapping tools: improved version released, *EOS, Trans. Am. Geophys. Un.,* **94**(45), 409–410.

Zamora, G. & Gil, W., 2018. The Marañón Basin: tectonic evolution and paleogeography, in *AAPG MEMOIR: Petroleum Basins and Hydrocarbon Potential of the Andes of Peru and Bolivia,* Vol. **117,** AAPG Special Volumes, G. Zamora; K. R. McClay; V. A. Ramos, eds Zamora, G., McClay, K.R. & Ramos, V.A., American Association of Petroleum Geologists.